Pacific Northwest
NATIONAL LABORATORY

PNNL-36772

Evaluation of DED and LPBF Fe-based Alloys Process Application Envelopes based on Performance, Process Economics, Supply Chain Risks, and Reactor-specific Targeted Components

M2CT-24PN1304052

September 2024

Isabella van Rooyen, Subhashish Meher, Asif Mahmud, Ankit Roy
Pacific Northwest National Laboratory

Srinivas Aditya Mantri, Xuan Zhang, Wei-Ying Chen
Argonne National Laboratory

U.S. DEPARTMENT OF ENERGY

Prepared for the U.S. Department of Energy
under Contract DE-AC05-76RL01830

DISCLAIMER

PACIFIC NORTHWEST NATIONAL LABORATORY
operated by
BATTELLE
for the
UNITED STATES DEPARTMENT OF ENERGY
under Contract DE-AC05-76RL01830

Printed in the United States of America

Available to DOE and DOE contractors from
the Office of Scientific and Technical Information,
P.O. Box 62, Oak Ridge, TN 37831-0062
www.osti.gov
ph: (865) 576-8401
fox: (865) 576-5728
email: reports@osti.gov

Available to the public from the National Technical Information Service
5301 Shawnee Rd., Alexandria, VA 22312
ph: (800) 553-NTIS (6847)
or (703) 605-6000
email: info@ntis.gov
Online ordering: http://www.ntis.gov

PNNL-36772

Evaluation of DED and LPBF Fe-based Alloys Process Application Envelopes based on Performance, Process Economics, Supply Chain Risks, and Reactor-specific Targeted Components

M2CT-24PN1304052

September 2024

Isabella van Rooyen, Subhashish Meher, Asif Mahmud, Ankit Roy
Pacific Northwest National Laboratory

Srinivas Aditya Mantri, Xuan Zhang, Wei-Ying Chen
Argonne National Laboratory

Prepared for
the U.S. Department of Energy
under Contract DE-AC05-76RL01830

Pacific Northwest National Laboratory
Richland, Washington 99354

Summary

The U.S. Department of Energy (DOE), Office of Nuclear Energy (NE), Advanced Materials and Manufacturing Technologies (AMMT) program aims to develop extreme-environment materials solutions for use in the deployment of advanced nuclear reactors and the sustainment of the current fleet. To achieve this objective, a combination of experimental methods, computational tools, and machine learning (ML) techniques for material design is employed to advance the maturation of materials for nuclear technology.

Through advanced manufacturing techniques such as laser powder bed fusion (LPBF) and laser powder direct energy deposition (LP-DED), components with complex geometries can be fabricated with reduced time and effort. Such advanced manufacturing methods can also provide the opportunity to improve materials performance through optimized microstructures and mechanical properties. However, existing engineering alloys are frequently unsuitable for additive manufacturing (AM) because their compositions have been optimized for fabrication via conventional methods. Thus, similar alloys with modified compositions that are better suited for AM can be studied for improved performance.

Over the past three years, the AMMT teams from Argonne National Laboratory (ANL) and Pacific Northwest National Laboratory (PNNL) studied various known Fe-based alloys by evaluating their initial printability using LPBF, and an AMMT-developed down-selection and decision matrix reduced the number of alloys to be studied from six to three in fiscal year (FY) 2024. Additionally, in FY 2024, for parallel evaluation, these three alloys were studied using LP-DED. While LPBF is better for small- to medium-sized components with high detail and internal features, LP-DED combines a material feed system to place the powder onto the exact spot where the laser will melt the material. This AM method can be easily scaled extremely large components and provides high build rate speeds compared to those of conventional LPBF systems. Additionally, DED is a better choice for complex geometries and compositional gradients.

The following three alloy systems were studied:

1. A709 is an advanced austenitic stainless-steel alloy. Extensive work has been performed on the wrought form because the DOE-NE Advanced Reactor Technology (ART) material down-selection program recommended it as a Class A structural material for sodium-cooled fast reactors (SFRs) because of its superior structural strength. There is no available literature on the AM aspects of A709; therefore, AMMT embarked on AM printability studies for additional benefits of AM deployment.
2. Grade 91 (G91) steel is included in ASME Boiler and Pressure Vessel Code (BPVC), Section III, Division 5. While there has been some work on the LPBF of G91 steel, there is a limited amount of work on DED-AM of this alloy to understand its microstructural evolution and mechanical behavior.
3. Grade 92 (G92) steel was developed as a 3rd-generation creep-resistant ferritic/martensitic (F/M) steel with the addition of tungsten. While it has been reported to have better creep properties relative to those of G91 steel, it has not been code qualified. Optimized Grade 92 (Opt.G92) steel was developed at Oak Ridge National Laboratory (ORNL) in support of the SFR program, which showed moderate enhancement in creep resistance with normal creep rupture ductility as compared to those of G92 and G91 steels. At the time when the AMMT program started, there was no available research on the AM of G92 steel.

The main conclusions for LPBF and LP-DED development are as follows:

- Larger-scale A709 alloys were successfully printed using LPBF based on a study from the previous year on optimizing the process parameters. The microstructural evolution of the alloy was studied after performing a series of heat treatments. The role of solution annealing led to insights regarding the need for different heat treatments for additively manufactured alloys compared to their wrought counterparts. Precipitation treatment of this alloy with and without prior solutionizing leads to the formation of a microstructure that contains different secondary and tertiary precipitates in the face-centered cubic (FCC) matrix, which significantly enhance the mechanical behavior, as noted from room- and elevated-temperature tensile testing.
- Similar observations were noted for the printing of the F/M steels (G91 and G92). A good combination of strength and ductility was obtained using a combination of different heat treatments for both alloys according to room-temperature tensile testing.
- The parametric study performed for LP-DED identified the processing window for the A709, G91, and G92 steels. Tensile samples of A709 were fabricated with a laser power of 400 W and a scan speed of 600 mm/min and were observed to be fully dense (99.97%). Tensile samples were fabricated with the optimized parameters. G91 tensile samples were fabricated using a laser power of 500 W, a scan speed of 600 mm/min, and a hatch spacing of 0.9 mm. G92 tensile samples were fabricated using a laser power of 500 W, a scan speed of 700 mm/min, and a hatch spacing of 0.9 mm.
- A chemical-composition-based ML model was used to predict the tendency of balling defect formation and the porosity of alloys produced by laser-based AM. The coupled ML and FLOW-3D results have provided insights into the impact of the alloy composition—particularly, the carbon content—on the printability of SS316L and SS316H during AM processes.
- This exercise proves that the AM of the selected current Fe-based reactor materials, either austenitic stainless steel or F/M steels, is very feasible, and more work needs to be done to understand the microstructural evolution during deposition and to further optimize the final microstructures.

LPBF- and LP-DED-processed A709, G91, and G92 steels were compared, although it should be noted that the body of research for LP-DED lags one year behind LPBF research, as funding and research only started FY 2024. Therefore, comprehensive performance comparisons could not be completed at this time. It is important to understand the role of processing routes on the overall microstructure of the samples printed to assess the final mechanical behavior and subsequently the applications to which these parts can be used. The main observations for as-deposited samples of the three alloys studied in this work are as follows:

- A709 Austenitic Stainless Steel: Inspection of A709 samples fabricated using both DED and LPBF in the as-deposited condition revealed that they both have a single-phase FCC crystal structure. The presence of cell boundaries, a typical feature in austenitic stainless steels, is also noted in both samples. The main differences between the two processes are more observable when looking at the grain sizes based on the electron backscatter diffraction (EBSD) inverse pole figures (IPFs). The DED sample has longer/more elongated grains compared to the those of the LPBF-processed sample. This could lead to more anisotropy when tested along the build direction as compared to testing across the build direction.
- G91 & G92 F/M Steels: In the case of the F/M steels, the difference between the two processes seems to be more pronounced. In the case of the LPBF sample, for the as-

deposited conditions, the microstructure seems to show more than a single-phase body-centered cubic (BCC) structure. Smaller precipitates, most likely theta, along with the presence of martensite-like laths are also observed in this sample. These features can be delineated based on the melt pool of the laser. For the DED samples, scanning electron microscopy (SEM) images and EBSD IPF maps show what appear to be martensite-like laths; however, only a BCC phase was noted from the X-ray diffraction (XRD) results. It should be mentioned here that, the body-centered tetragonal (BCT) phase (martensite) overlaps with the BCC phase, so it is possible that we may not be able to see the martensite phase even if its present.

Future recommendations for LPBF and LP-DED work focusing on A709 and G92 alloys (G92 is being pursued because of its improved properties compared to those of G91) include the following:

1. FY 2025 will focus on further understanding the microstructural evolution and mechanical behavior (room and elevated temperature) of AM samples compared to the wrought materials.
2. The mechanical properties of as-fabricated LP-DED AM samples will be assessed, and additional heat treatments based on lessons learned from the prior years' work on LPBF will be carried out. However, the heat-treated LPBF samples will receive further attention: a solution annealing treatment at a minimum temperature of 1150°C for 10 hours will be implemented, followed by air cooling. A precipitation treatment (PT) will be carried out at 775°C for 10 hours in air, followed by air cooling. Future study will focus on room-temperature tensile testing for DED-fabricated A709 and G92 alloys. In addition, detailed electron microscopy analyses after the heat treatments and tensile testing also fall within the work scope.
3. The Flow-3D software will be coupled with ML for extensive research on the role of the chemical composition on the printability using the DED process.

A brief preliminary overview of business value considerations is given for the deployment of these AM techniques and decision-making regarding choices related to the product–AM technique combination. Considering that little information has been quantified or validated, a supply chain evaluation needs to be urgently carried out in the nuclear community by economic and systems specialists.

This research work performed at ANL and PNNL is also published and presented: (1) one invited conference talk, (2) two accepted conference presentations, (3) one peer-reviewed paper published in the reputable journal *Materialia*, and (4) one paper already submitted and three being drafted.

Finally, it is concluded that all three material types have to the potential to be manufactured using both LPBF and LP-DED. However, it should be noted the process optimization was achieved within a limited parameter window and has not yet been fully "optimized." Different geometries may also necessitate modifications to the parameters and the parameter sets described in this works, needs to be confirmed for different geometries and size scales. All mechanical properties and relationship with post heat treatment have not been fully examined and is recommended to be completed before a final decision has been made. It is recommended that future studies focus on A709 and Grade 92 only, to have focus on one austenitic and one ferritic/martensitic material type.

Acknowledgments

The research presented here was supported by the Advanced Materials and Manufacturing Technology (AMMT) program of the DOE Office of Nuclear Energy. PNNL is a multi-program national laboratory operated for the U.S. Department of Energy (DOE) by Battelle Memorial Institute under Contract No. DE-AC05-76RL01830.

Dr Carolyne Burns is thanked for the peer review and Isaiah Steinke for the technical editing of this report. Daniel Yoon is acknowledged for his assistance with SolidWorks.

We would like to acknowledge Prof. Xiaoyuan Lou and PhD students John Snitzer and Qianwen Zhang from Purdue University for the laser directed energy deposition of A709, Grade 91, and Grade 92 alloys on behalf of PNNL.

We would like to acknowledge Stephanie Barbara Lawson (PhD student), Somayeh Pasebani (Professor) at Oregon State University for their support in the use of Flow-3D software for printability study.

The following researchers contributed towards the reporting of the research performed as part of the Innovative Nuclear Materials program and is specifically acknowledged towards the technical work performed:

- Meher, S., Ankit Roy, Asif Mahmud, Peter A Renner, Chinthaka Silva, Mohan SKKY Nartu, Ariel Rieffer, German A Valenzuela, Isabella J van Rooyen. 2024. Studies on Printability Methodologies and Directed-Energy-Deposition-Fabricated Iron Alloys for Nuclear Applications, PNNL-36408. M3CT-24PN1304051, August 2024.

- Mantri, S. A., Xuan Zhang, Wei-Ying Chen. 2024. Laser Powder Bed Fusion of Steels for Nuclear Applications. ANL-AMMT-017, August 2024.

Acronyms and Abbreviations

AFSD	Additive Friction Stir Deposition
AM	Additive Manufacturing
AMMT	Advanced Materials and Manufacturing Technologies
ANL	Argonne National Laboratory
ART	Advanced Reactor Technology
BCC	Body-Centered Cubic
BCT	Body-Centered Tetragonal
BPVC	Boiler and Pressure Vessel Code
DED	Directed Energy Deposition
DOE	U.S. Department of Energy
EBSD	Electron Backscatter Diffraction
F/M	Ferritic/Martensitic
FC	Furnace Cooling
FCC	Face-Centered Cubic
FGM	Functionally Graded Materials
FY	Fiscal Year
G91	Grade 91
G92	Grade 92
HIP	Hot Isostatic Pressing
INL	Idaho National Laboratory
IPF	Inverse Pole Figure
LMD	Laser Metal Deposition
LPBF	Laser Powder Bed Fusion
LP-DED	Laser Powder Directed Energy Deposition
LWR	Light Water Reactor
ML	Machine Learning
NE	Office of Nuclear Energy
Opt.G92	Optimized Grade 92
ORNL	Oak Ridge National Laboratory
PNNL	Pacific Northwest National Laboratory
PSD	Particle Size Distribution
PWR	Pressurized Water Reactor
SEM	Scanning Electron Microscopy
SFR	Sodium-Cooled Fast Reactor
SR	Stress Relieving
ST	Solution Treatment

TEM	Transmission Electron Microscopy
UTS	Ultimate Tensile Strength
VED	Volumetric Energy Density
XRD	X-Ray Diffraction
YS	Yield Strength

Contents

Figures

Tables

1.0 Introduction

The U.S. Department of Energy (DOE), Office of Nuclear Energy (NE), Advanced Materials and Manufacturing Technologies (AMMT) program aims to develop extreme environment materials solutions for use in the deployment of advanced nuclear reactors and sustainment of the current fleet. To achieve this objective, a combination of experimental methods, computational tools, and machine learning techniques for material design is employed to advance the maturation of materials for nuclear technology.

Through advanced manufacturing techniques such as laser powder bed fusion (LPBF) and laser powder direct energy deposition (LP-DED), components with complex geometry can be fabricated with reduced time and effort. Such advanced manufacturing methods can also provide opportunity to improved materials performance through optimized microstructures and mechanical properties. However, existing engineering alloys are often well-suited for fabrication with additive manufacturing (AM), as their compositions have been tuned to optimize fabrication via conventional methods. Thus, similar alloys with modified compositions that are better suited for additive manufacturing can be studied for improved performance.

Adoption of such advanced composition and manufacturing methods for well-known alloys can serve materials requirement for nuclear reactors via 1). Reduced neutron activation due to added elements and 2). Unique microstructures due to thermal cycles associated with AM process. It is common to encounter many challenges such as high susceptibility to defects and microstructure inconsistencies during AM processes. This poses a significant challenge of obtaining optimal processing parameters for an alloy not previously investigated. Thus, there are requirements for efficient frameworks to efficiently and effectively determine the processing parameter window of a given alloy considered as potential feedstock for AM. An ideal framework integrates experiments, physics-based simulation, uncertainty analysis and fabrication and characterization to determine the bounding region in the manufacturing space resulting in near full density, defect-free parts.

AM generally refers to a process in which an engineering component is built in a layer-by-layer fashion close to their final (net) shape. This design flexibility along with the potential for powder reuse, reduced waste, cost, and manufacturing steps (i.e., rapid prototyping) provides certain advantages over components that are traditionally manufactured (Lewandowski and Seifi, 2016). However, anisotropy in microstructures and mechanical properties, high residual stresses generated due to large thermal gradient yielding distortion and cracking of parts, and porosity often results in optimization and post processing of the as-fabricated AM alloys. In recent times, there have been significant efforts to explore the feasibility of employing AM techniques for the manufacturing of components in energy sector particularly incorporation of current reactor materials via the Advanced Materials and Manufacturing Technologies (AMMT) roadmap (Li et al., 2023). IN FY2023, four US National Labs: ANL, ORNL, PNNL, and INL worked in tandem to down select some of the current reactor materials that have the potential to benefit from AM technique.

1.1 Material Choice

A variety of material types and advanced manufacturing processes are being evaluated by the AMMT program (Figure 1). Discussed here, is aspects regarding the Fe-based material development performed by Argonne National Laboratory (ANL) and Pacific Northwest national Laboratory (PNNL).

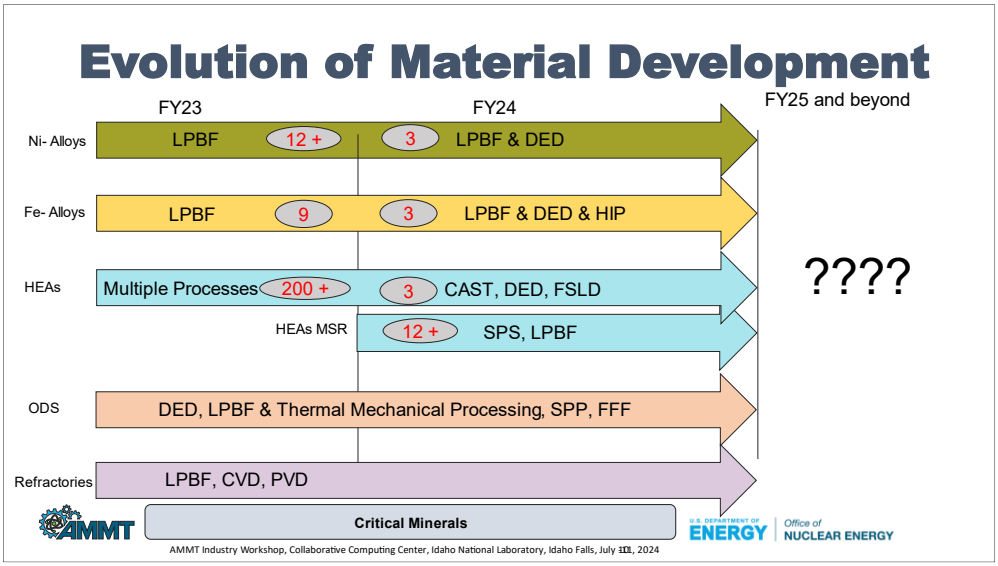

Figure 1. Industry interest in AM techniques based on the GIF-AMME WG 2023 industry survey (Van Rooyen, 2024a).

The AMMT teams from ANL (Mantri and Zhang, 2023 and Mantri et.al. 2024) and PNNL (Meher et al. 2023, 2024) have studied over the past three years various known Fe-based alloys by evaluating its initial printability using LPBF and using an AMMT developed down selection and decision matrix from six alloys to three alloys to be studied in FY 24. Additionally, in FY 24, for parallel evaluation, these three alloys were also studied using LP-DED. While LPBF is better for small to medium-sized components with high detail and internal features, DED combines a material feed system to place the powder onto the exact spot where the laser will melt the material. This AM method can be easily scaled to extremely large components along with high build rate speeds when compared to conventional LPBF systems. Additionally, DED is a better choice for complex geometries and compositional gradients.

The concept of a decision matrix was developed to expedite the development and implementation of new and existing materials for use in a nuclear reactor. During the initiation stages of the AMMT program, material score cards (Hartmann and Devanathan 2021 and Hartmann et al. 2022) were developed to categorized and prioritized material development needs. While the two phased score cards provided realistic insights into the overall technical maturity of AM nuclear materials, the decision criteria employed were broad and did not capture all key aspects. Therefore, considering the knowledge gaps and key stakeholder inputs, the decision criteria were revised and elaborated to reflect more specific elements. The revised decision criteria matrix was utilized to perform the down selection from six to three alloys to be studied in FY24. These three alloys are the austenitic stainless steel: A709, and ferritic/martensitic steels: Grade 91 and Grade 92 (henceforth referred to as G91 and G92 respectively).

The key reason for the down selected materials as follows:

- The high-temperature tensile properties, thermal stability, creep strength, creep-fatigue resistance, sodium compatibility, and weldability for A709 and other stainless steels such as 316H were compared in a previous study (Sham et al. 2022). A709 exhibits the best overall performance, as illustrated in the property ranking chart in Figure 2. A DOE-NE advanced Reactor Technology (ART) material down-selection program recommended A709, an

advanced austenitic stainless-steel alloy, as a Class A structural material for the Sodium cooled Fast Reactor (SFR) because of its overall superior structural strength advantage (Sham et al. 2022). Extensive work has been performed on wrought A709 form to have it code-qualified, but there is no available literature on the additive manufacturing aspects and therefore AMMT embarked on these initial printability studies.

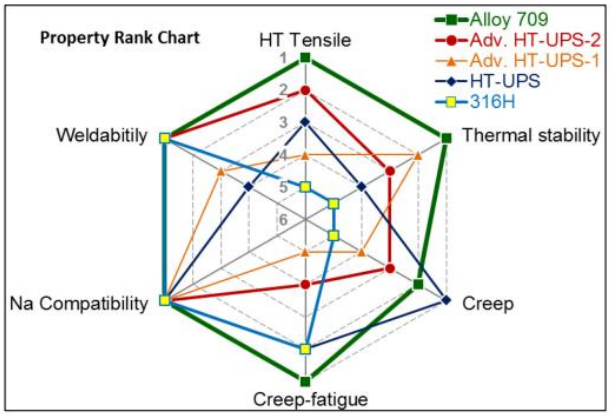

Figure 2. Property ranking chart for A709, HT-UPS, its variants, and Type 316 stainless steels. A709 shows the best overall performance (Sham et al. 2022).

- Grade-91 steel (henceforth referred to as G91) is broadly used in fossil and nuclear power plants in components operating at temperatures up to ~650 °C. This alloy is also included in ASME Boiler and Pressure Vessel Code (BPVC) Section III Division 5. While there has been some work on the LPBF of Grade 91 steel (El-Atwani et al. 2021; Eftink et al. 2021), limited amount of work on DED-AM has been explored to produce this alloy to understand the microstructural evolution and mechanical behavior (Hatakeyama et al. 2023; Samuha et al., 2023; Tan et al. 2022; Zhong et al. 2021).
- To improve the creep properties of 2nd generation G91 alloy, Grade 92 steel [G92] was developed as a 3rd generation creep-resistant F/M steel with the addition of tungsten (Hasegawa, 2014). While it has been reported to have better creep properties relative to Grade 91, it has not been code qualified (Abe 2008). Tan and Chen (2021) reported the long-term thermal aging effect evaluation for G92 steel at LWR relevant temperature. Blocks of G92 steel were aged at 350 °C for 12.6-12.7 kh and 36-37 kh. In general, no significant change in microstructure was observed except for some development of Laves phase (~100-200 nm), however, the aging resulted in some reduction in hardness and YS/UTS with a little increase in ductility for the 36-37 kh aged G92. In addition, optimized Grade 92 [Opt.G92] steel was developed at ORNL in support of the Sodium-cooled fast reactor program which showed moderate enhancement in creep resistance with normal creep rupture ductility as compared to G92 and G91 steel (Tan et al. 2017; Tan 2018). As of now, there is no available research on the additive manufacturing of G92 steel. At the time when the AMMT program started, there was no available research on the additive manufacturing of Grade 92 steel.

In the financial year (FY)-23, a chemical composition-based machine learning model has been developed to predict the printability of any given alloy in LPBF using experimental data from peer-reviewed literature. This was expanded in FY24 to focus on composition effects on printability of 316 L and 316 H as well as considering differences between LPBF and DED. A brief will be provided in Section 3.4

1.2 Choice of Manufacturing Method

The laser powder bed fusion (LPBF) research is being carried out for these three alloy at Argonne National Laboratory (ANL). At PNNL, the powder-based DED (henceforth referred to as LP-DED) research of the three alloys were carried out in collaboration with Purdue University.

While LPBF is better suited for small to medium-sized components with intricate details and internal features, the DED method can be easily scaled to extremely large components along with high build. Additionally, DED is a better choice for functionally graded materials (FGM). Figure 3 presents the selection of AM processes based on overall build volume. LPBF has the maximum build height of 1 m and build diameter of 1 m while LP-DED has a maximum build height of 3 m and build diameter of 2m. In general, the greatest aspect ratios were observed for DED processes and the smallest are for cold spray (Gradl et al. 2022).

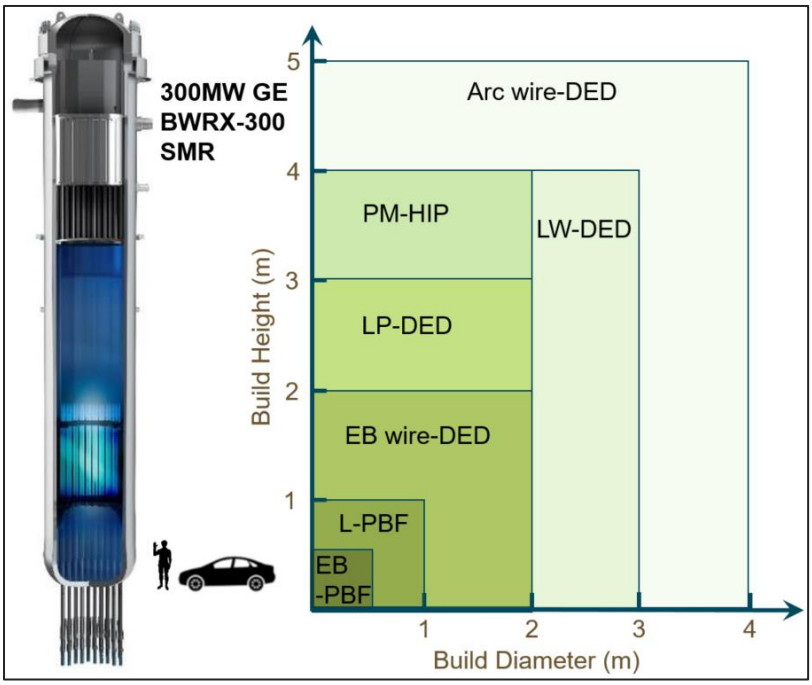

Figure 3. Dimensional application space for various AM processes as adapted from (Gradl et al. 2022).

The GIF-AMME-WG 2023 industry survey showed a significant increased interest in DED with 19 industry references to wire-fed DED and 15 to powder-fed DED, which is a significant increased interest compared to the survey conducted during 2023 (Figure 4). Furthermore, the AMMT program (Li et al. 2023) has already significant investment in the acceleration and demonstration of LPBF (also listed in Figure 4 as one of the top five AM techniques), and nationally and internationally many organizations already perform research and development with demonstrations of applications, although not with the material identified namely A709, G91 and G92. Therefore the AMMT program decided to pursue both LP-DED and LPBF as a manufacturing technique that can benefit nuclear energy stakeholders, Although wire-DED is of interest for scaling up and even larger applications, the AMMT decided to evaluate first the powder based processes (some selected wire-DED demonstration work is however in process as part of a separate AMMT project and selected Ni-based wire DED is currently been

undertake on Ni-alloy 282). In addition to the potential for larger scale products and manufacturing rate increases, it also provides additionally the opportunity for more complex geometries and robotically features.

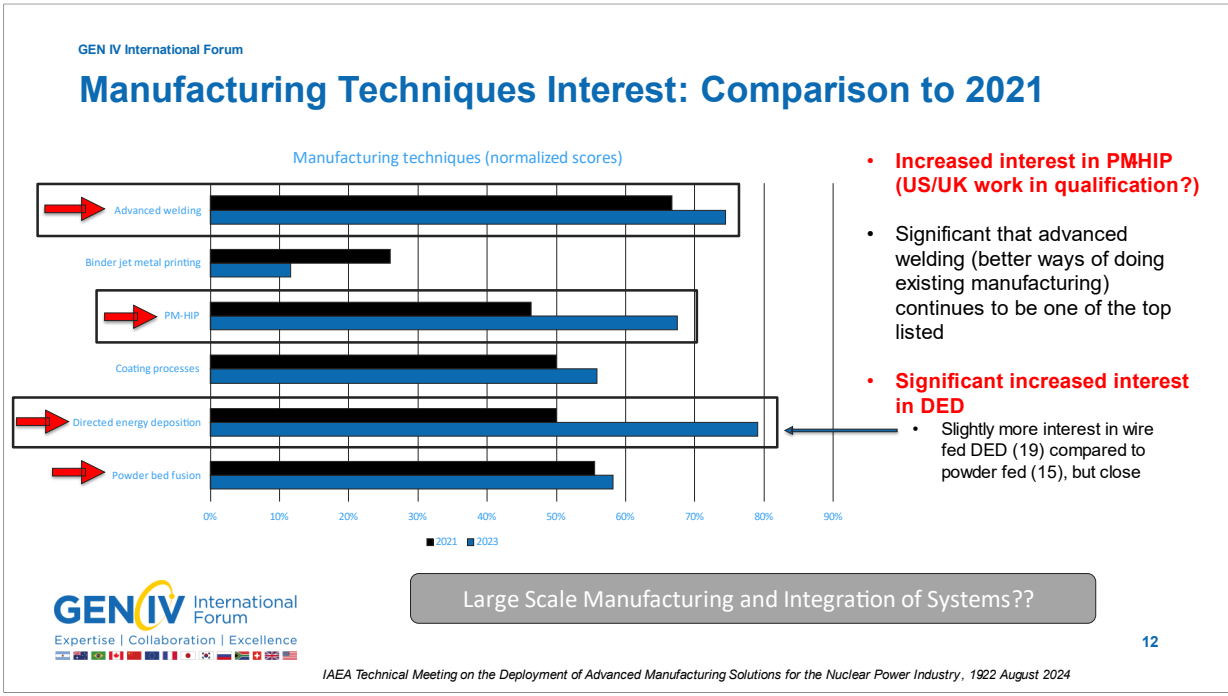

Figure 4. Industry interest in AM techniques based on the GIF-AMME WG 2023 industry survey (Van Rooyen et al. 2024b).

1.3 Objectives

The objective is to compare DED and LPBF Fe-based alloys process application envelopes based on performance, process economics, supply chain risks, and reactor-specific targeted components.

The Printability Machine Learning Study objectives are multi-faceted and aim to address various aspects of additive manufacturing. The primary objective is to identify optimal alloy compositions that exhibit enhanced printability and minimum defects like porosity, balling, warping, and cracking. These objectives align well with the goals of the AMMT program to enhance the printability of the existing materials thereby accelerating the deployment of advanced manufacturing processes. The secondary objective is to characterize printability factors and investigate how different alloy compositions influence key factors affecting printability, including fluid flow dynamics, heat transfer, solidification behavior, and microstructure formation.

1.4 Scope of Work

This work package supports the vision and goals of the AMMT program relevant to accelerate the development and deployment of advanced manufacturing processes. Achieving this, can provide a safety improvement through larger safety margins, economic benefit for higher efficiency during operation and a cost reduction through more cost-effective manufacturing processes and less waste.

The scope of this work is specifically to deliver a PNNL-ANL interlaboratory evaluation identifying DED and LPBF Fe-based alloys process application envelopes based on performance, process economics, supply chain risks, and reactor-specific targeted components.

Specifically, the following is discussed:

- Section 2: Briefly the main characteristics and fundamental changes between the two processes are discussed as that will direct decision making for future applications. This includes the main parameters, powder characteristics, and process fundamentals.
- Section 3: Performance of LPBF and LP-DED Products: AMMT Program Experimental Research Case Study: A summary of recent research and development results from A709, G91 and G92 performed by ANL and PNNL is provided in this section. Additionally, a summary of the printability ML framework is provided.
- Section 4: A brief preliminary overview is provided on some of the business value considerations that need to be addressed for deployment of these AM techniques and for decision-making regarding the choice of product-AM technique combinations.
- Section 5: A summary and recommendations are provided in this section.
- Section 6: All project deliverables including publications, presentations and future works are listed in this section.
- Lastly, the references are listed in Section 7.

2.0 Process Description

Briefly the main characteristics and fundamental changes between the two processes are discussed as that will direct decision making for future applications.

2.1 Physics of Differences in the LPBF and LP-DED Processes

Figure 5 presents the detailed schematic of LPBF and LP-DED processes. In general, most of the incident heat energy in DED process is transferred via conduction through the deposited structure. At the bottom of the sample, heat is conducted away easily via the substrate while convection and radiation predominate at the top of the sample. In general, due to temperature gradients, cooling rates and repeated heat treatments during subsequent laser-deposition, heterogenous microstructure can be observed in different regions of the sample which in turn can influence the mechanical properties (Alcisto et al. 2010; Selcuk 2011; Shamsaei et al. 2015).

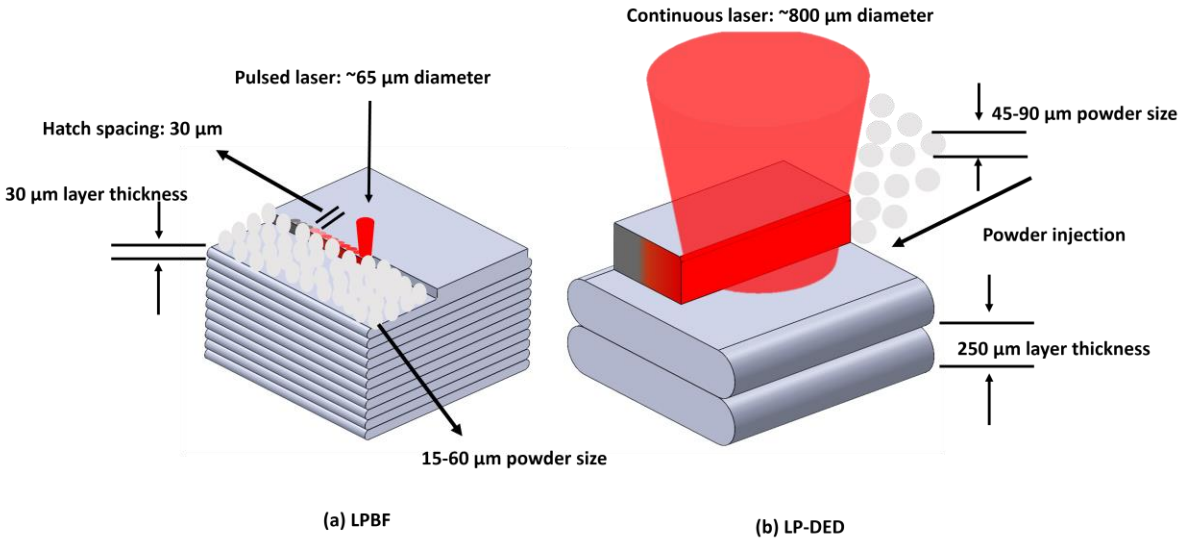

Figure 5 Schematic of the fabrication process of (a) LPBF, and (b) LP-DED (Babuska et al. 2021).

The primary LPBF processing parameters are laser power, laser scan speed, hatch spacing, slice thickness/layer thickness, which in general is expressed in terms of volumetric energy density (VED) (Bertoli et al. 2017a). VED is defined as:

$$\text{VED} = \frac{Laser\ power\ (W)}{Laser\ scan\ speed\ \left(\frac{mm}{s}\right) \times hatch\ spacing\ (mm) \times slice\ thickness\ (mm)} \ (\text{J/mm}^3)$$

In addition, layer rotation and scanning strategies are also considered. The build is generally performed under an inert atmosphere and the build plate is typically preheated (25-200 °C) to reduce internal/residual stress.

The important parameters for the LP-DED processes are powder feed rate, laser power, laser scan speed, layer thickness, laser scanning strategy, and flow rate of shielding gas used. These parameters influence the incident energy, melt pool shape, cooling rate and thermal gradients

which in turn play a critical role in the final microstructure and residual stress of the fabricated components (Sames et al. 2016).

Babuska et al. (2021) investigated the mechanical performance of Fe-Co alloy additively manufactured by LPBF and LP-DED and compared it with conventional wrought alloy. Tensile testing of the Fe-Co alloy fabricated by LPBF revealed higher strength (500–550 MPa) and high ductility (35 %) while low strength (200–300 MPa) and low ductility (~2.7 %) were observed for the alloys fabricated via DED. These differences in mechanical properties were attributed to the unique thermal history involved in the two processes. It should be mentioned that Fe-Co is considered an intermetallic alloy with low strength (200-400 MPa) and low ductility (~4%) when conventionally manufactured (Sourmail 2005). Further investigation is needed to determine whether these differences in mechanical properties are observed in other low to high strength alloys when manufactured by both LPBF and LP-DED.

Baig et al. (2024) investigated the tensile behaviors of Haynes® 214 with a wide range of temperatures (-195 to 980 °C) fabricated via both LPBF and DED processes. They reported higher strength for the LPBF specimens compared to the DED specimens up to 650 °C primarily due to the presence of finer grain size of the LPBF specimens. However, ductility was observed to be similar for both processes up to 650 °C and the reported failure was due to transgranular fracture in both processes. The comparable ductility up to 650 °C was attributed to the heterogeneous grain size distribution observed in the LPBF and DED processes. It needs to be mentioned that before testing, the L-PBF and LP-DED specimens were heat treated following a 3-step procedure which consisted of stress relieving (SR) at 1065 °C for 1.5 h in vacuum with furnace cooling (FC) followed by a hot isostatic pressing (HIP) cycle at 1163 °C/100 MPa for 3.5 h in argon and, finally, solution treatment (ST) at 1100 °C for 2 h with argon quench (AQ).

(Gnasse et al. 2023) reported a comparative study on the mechanical properties of high-strength tool steel 1.2709 additively manufactured via laser metal deposition (LMD) and LPBF. They observed no significant differences in the mechanical properties of the as-built 1.2709 tool steel processed via both LMD and LPBF. However, they observed a higher yield strength (22% higher) and higher UTS (19% higher) after heat treatment for specimens manufactured via LPBF compared to those processed by LMD. In contrast, specimens fabricated by LMD exhibited higher Young's modulus (6% higher) and increased ductility (27% more) compared to LPBF after heat treatment. These variation in mechanical properties after heat treatment were attributed to the differences in microstructure observed in the LMD and LPBF process owing to differences in thermal history, heat input and cooling rate. Their study revealed that LMD manufactured components are more suitable for use where higher stiffness is required while LPBF processed components are more suitable where greater strength is important.

2.2 Critical Parameters for Both Processes

LP-DED and LPBF processes have both their advantages and limitations (Bertoli et al. 2017b; Haley et al. 2021; King et al. 2015; Thompson et al. 2015). A comparative analysis of LP-DED and LPBF is presented in Table 1.

Table 1. Comparison between LP-DED and LPBF processes.

Parameter	LP-DED	LPBF
Deposition rate	0.1-5 kg/h	10-100 g/h
Linear deposition volume	0.3-1.5 m	0.1-0.5 m
Typical layer thickness	~250 µm	10-50 µm
Melt pool size	500 µm-1 cm	~100 µm
Minimum feature size	~380 µm	75-100 µm
Cooling rate	10^3–10^4 K/s	10^5–10^7 K/s
Resolution	Low	High
Feedstock efficiency	30-90+ %	>50% (with recycling)
Feedstock cost	Med-high	Med-high
Atmosphere	Glovebox, flowing shielding gas	Glovebox
Surface roughness	Medium	Low
Nozzle for feedstock orientations	Coaxial, multiple nozzles	Not applicable
Hybrid CNC milling integration	Available	Not applicable
Multi-materials printing	Available	Not applicable
Overhanging Structures	Difficult to fabricate	Certain advantages
Capital expense	Medium	High

2.3 Powder Size

Careful consideration should be taken for feedstock selection for both LP-DED and LPBF processes. In general, due to the lower laser spot size (~75 µm) of the LPBF process, the optimum powder size is e around ~15-50 µm with the powders being spherical in shape. Powder sizes of ~50-150 µm can be employed for the DED process due to comparatively higher laser spot size. In addition, microstructure, powder morphology, particle size distribution, elemental composition, free flowing, internal porosity should be taken into consideration while selecting the feedstock. In general, the powder characteristics (i.e., D10, D50, and D90) can be

obtained from the OEM or powder manufacturer (typically produced via gas or water atomization), however, it is recommended to investigate the powder morphology via SEM and EDS. The powder size distribution is typically narrowed by sieving. SEM can be used to investigating the powder surface morphology i.e., cross-sectional microstructure, shape and size, and presence of satellites while elemental composition of the powders can be estimated from EDS (Chowdhury et al. 2022; Haley et al. 2021).

Another important aspect is the powder reuse and powder recycling during AM process. Numerous studies have investigated the powder recycling and impacts of powder reuse on the mechanical properties of the fabricated alloy (Alamos et al., 2020; Ghods et al., 2021; Santecchia et al. 2020). In general, the three most common powder reuse methods are the single batch and collective aging methods, the top up method, and the refreshing method (Warner et al., 2024). Some important features to consider during powder recycling are flowability, porosity, oxygen pickup, moisture, powder sphericity, and total build time. In addition, the characteristics of powders differ from one manufacturing method to another and can impact the powder recycling process (Moghimian et al. 2021). Delacroix et al. (2022) investigated gas atomized 316L SS powder up to 15 times (virgin powder was used initially, recovered, sieved, and reused) in a standard LPBF process. They reported a slight increase in particle size with recycling, increased oxygen content, enhanced powder flowability and decrease in parts density. No significant differences in microhardness and tensile properties were observed with powder recycling. However, phase transformation was observed and a significant amount of δ-ferrite (~4 wt.%) was observed in the 15-times recycled powder after sieving, compared to the austenitic virgin powder (0–1 wt.% of BCC ferrite).

Variations in humidity, O_2 and CO_2 can alter the powder chemistry. In addition, history of the powder from the manufacturing and packaging at the factory to exposure to the environment where it will be used can have a significant impact on the powder chemistry for sensitive materials (rare earth metals and alloys) (Zach et al. 2023). Zach et al. (2023) reported three methods of powder production for specialty materials and materials that cannot be produced in large batches. The three methods are aerosol jetting, CNC machining, and ultrasonic atomization. Aerosol jetting can be used for materials that have low reactivity to air, water, and graphite. Zn, Yb, Ag, Cu, and Ru powders can be produced via CNC machining, however, this process requires further optimization for achieving higher efficiency/recovery. Ultrasonic atomization was determined to be the effective technique for production of small quantities of metals and alloys as this technique can produce spherical powder with tight particle size distribution (PSD). Example includes Si, Ag, Ti, Yb, and SiGe metals and alloy powders.

2.4 Wire DED

Although no wire DED research has been performed under this project, a brief discussion is produced as wire DED is also used to produce large-scale parts. Currently there is no literature available for the Wire DED of A709 alloy. On the other hand, there have been a couple of reports on the production of Grade-91 alloy via Wire DED. Work done by Oak Ridge National Laboratory reports that the microstructure was very similar the ones seen in the blown powder DED process, i.e. δ-ferrite matrix containing martensitic laths and MX (both nitrides and carbides) precipitates (Green et al. 2022; Li et al. 2021; Robin et al. 2024; Wang et al. 2024). For this work, US Welding Corporation provided the wire.

3.0 Performance of LPBF and LP-DED Products: AMMT Program Experimental Research Case Study

A summary of recent research and development results from A709, G91 and G92 performed by ANL and PNNL is provided in this section. A summary is also provided on the printability ML framework is provided.

3.1 Compositions (wt%) of A709, G91, and G92 Steel Powders Used to Fabricate LPBF and LP-DED Builds

The three alloy powders were purchased, and the manufacturers reported powder chemistry for each of the alloys are presented in Table 2.

Table 2. Manufacturers reported powder chemistry for LPBF and LP-DED builds.

	B	C	Cr	Fe	Mn	Mo	N	Nb	Ni	Si	V	W
A709	0.009	0.04	20.6	Bal.	0	1.4	0.15	0.3	25	0.1	0	0
Grade 91	0	0.07	8.5	Bal.	0.4	0.94	0.06	0.07	0	0.3	0.19	0
Grade 92	0	0.09	8.8	Bal.	0.4	0.4	0.09	0.08	0	0	0.19	1.7

3.2 LPBF of A709, G91, and G92 Steels

The results from each alloy will be presented following the same structure. The microstructure of the as-deposited sample will be shown in detail using advanced characterization techniques like scanning electron microscopy, EDS/EBSD, and transmission electron microscopy. This will be followed by the microstructure analyses of the heat-treated samples. Finally, the mechanical behavior of these alloys following room and elevated temperature tensile testing will be discussed (Mantri and Zhang 2023; Mantri et al. 2024).

3.2.1 LPBF of A709 Austenitic Stainless Steel

To understand the role of solution annealing on the additively manufactured A709, the samples were aged for different temperatures and times. Figure 6 shows the EBSD IPF maps of all 4 conditions, both across and along the build directions. In the as-deposited condition, slightly elongated “U-shaped” grains were observed along the build direction with sizes ranging from 10 µm microns to 120 µm with an average grain size of 40 microns. The “checkerboard” pattern noticed in the IPF maps perpendicular to the build direction is due to the scanning pattern employed during the deposition process. The grains are about ~30 microns in size. Annealing this sample at 1150 °C/1H did not influence either the grain morphology or size in both vertical and horizontal samples. The grain sizes from the EBSD analysis parallel and perpendicular to the build direction were noted to be ~40 and ~30 microns respectively. Finally, the samples that were annealed at 1200°C start to show a difference. After 2H, the grain size slightly increased in both samples. In the vertical sample, the grains start to lose the “U” shape and the size increased up to 50 microns. A similar change in the grain morphology was noted in the horizontal sample, breaking down the checkerboard pattern. A few annealing twins also start to form in this sample and have been highlighted in the Figure 6. This shows that the samples are

still only partially recrystallized, and possibly longer annealing times might be required to fully recrystallize the samples (Fan et al. 2024).

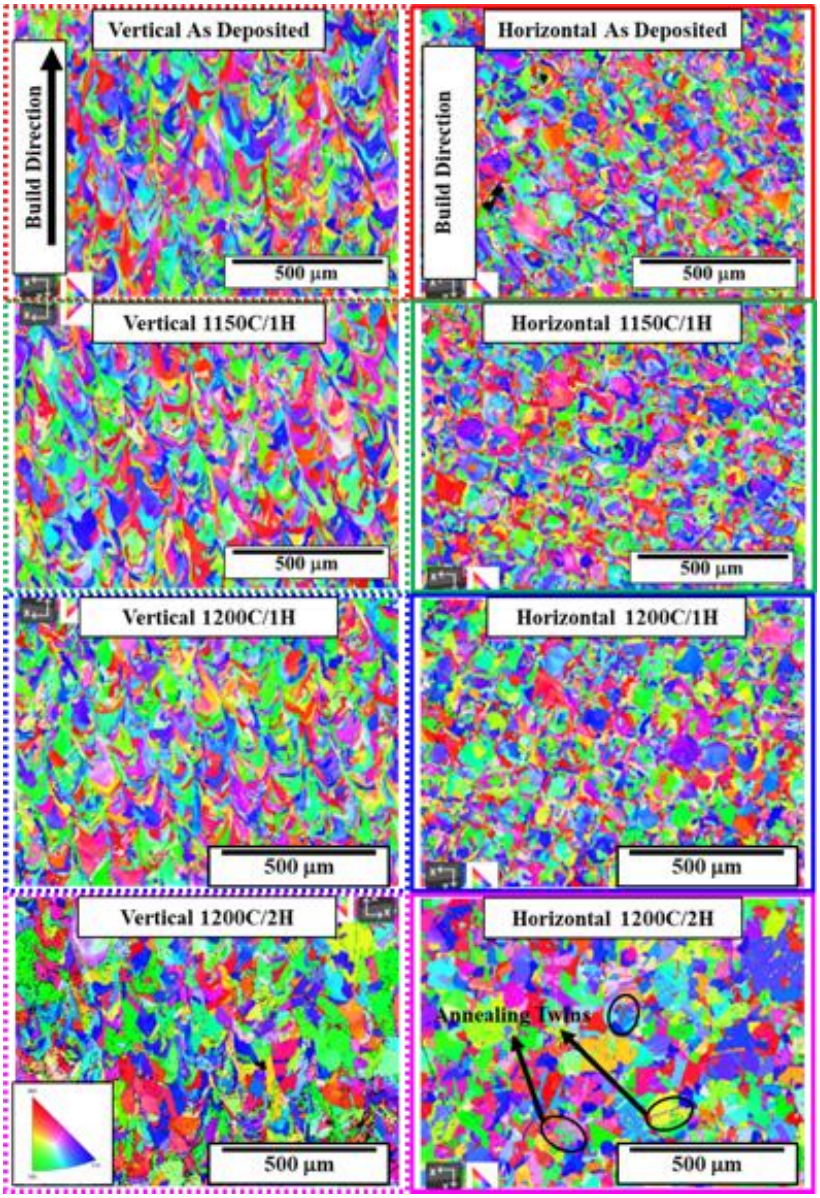

Figure 6. EBSD IPF maps of alloy A709 along and across the build direction after different solution annealing times.

Figure 7 shows these different microstructures obtained via TEM and puts them in comparison with the as-deposited sample. The BFTEM image in (a) and (b) do not clearly reveal the presence of any secondary phases. The SADP obtained along [001]γ, shown as inset, confirms this. No superlattice spots corresponding to any secondary phases are present. The BFTEM shows a very high density of dislocations present in the system. The dislocation cells can also be clearly observed. Following this, based on the work by (Natesan and Sham 2017; Sham et al. 2022), the as-deposited samples were then solution annealed at 1150 °C/1H. The presence of secondary phases is clearly noted. Based on the SADP analysis in Figure 7, these precipitates are determined to be MX carbonitrides, which are around 50 nm in size. MX

precipitates also have an FCC crystal structure, and have an orientation relationship with the matrix, i.e. [001]γ // [011]MX (Ding et al. 2019). The precipitates are mostly lined up near the dislocations and seem to be pinning them. It has been reported in literature that the dislocations act as nucleation sites for these MX precipitates (Sourmail and Bhadeshia 2005). The presence of these MX carbonitrides on the dislocations is known to provide good creep resistance. Interestingly though, a high number of dislocations are still present which indicates the heat treatment was not totally effective. As such, the as-deposited samples were further annealed at 1200 °C for 1H and 2H as shown in the Figure 7. The BFTEM images at different magnifications, reveal the presence of MX-carbonitrides in the γ-matrix. The overall size of these MX precipitates seems to be slightly larger in the samples aged at 1200 °C/2H than the ones noticed in 1150 °C/1H with some of the precipitates being as large as 100 nm. In the specific areas captured in this micrograph, the overall number also seems to be higher. Another noteworthy observation in these micrographs is the presence of what appears to be “fishnet” type of dislocations. These dislocations seem to be trapping the precipitates within them, which during deformation, could enhance the overall mechanical properties.

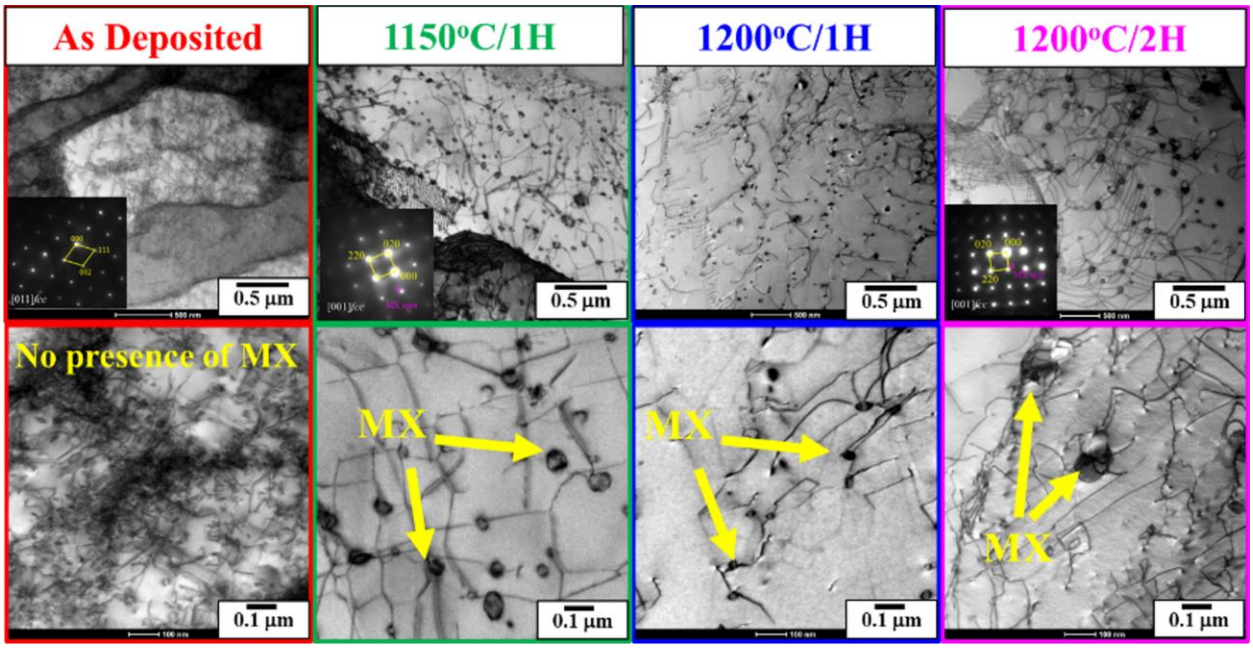

Figure 7. TEM of as-deposited A709 sample compared to the solution annealing at different temperatures and times.

Following the microstructural analysis, to understand the effect of these heat treatments on the mechanical behavior, room and elevated temperature tensile tests were performed on the samples, both along and across the build direction. The mechanical behavior of these samples is summarized in Figure 8. The engineering stress vs strain plot for the samples tested at room temperature are shown in Figure 8a. All the samples tested across the build direction show a greater yield and ultimate tensile strength compared to samples tested along the build direction. The as-deposited samples showed the highest strength with yield strength around ~665 MPa and UTS of ~790 MPa. Though the as-deposited samples had the highest strengths, their ductility were lower compared to the aged samples. With an increase in the aging time, the strengths decreased while the ductility increased. The sample aged at 1150 °C/1H showed a yield strength of ~490 MPa and UTS of ~710 MPa while the sample aged at 1200 °C/2H had a yield strength of ~300 MPa with UTS reaching ~610 MPa. These values are to be expected

when we look at the overall microstructures of these samples. The as-deposited sample with the highest number of strain/dislocations also has the higher YS/UTS and with aging, along with the stress relief, there is a change in the overall grain size which reduces the strengths. Another noteworthy observation is that aging the sample results in an increase in the strain-hardenability of the alloy. On the other hand, the wrought material has YS of ~300 MPa and UTS of ~650 MPa with strain to failure of ~55%. Following the room temperature tests, the samples were also tested at 550°C, these are shown in Figure 8b. As anticipated, the overall strengths of the alloy decreased with an increase in the testing temperature. YS/UTS dropped by ~150 MPa for all conditions, with no significant change in the ductility. It should be noted that the scale bars shown on the graphs are different.

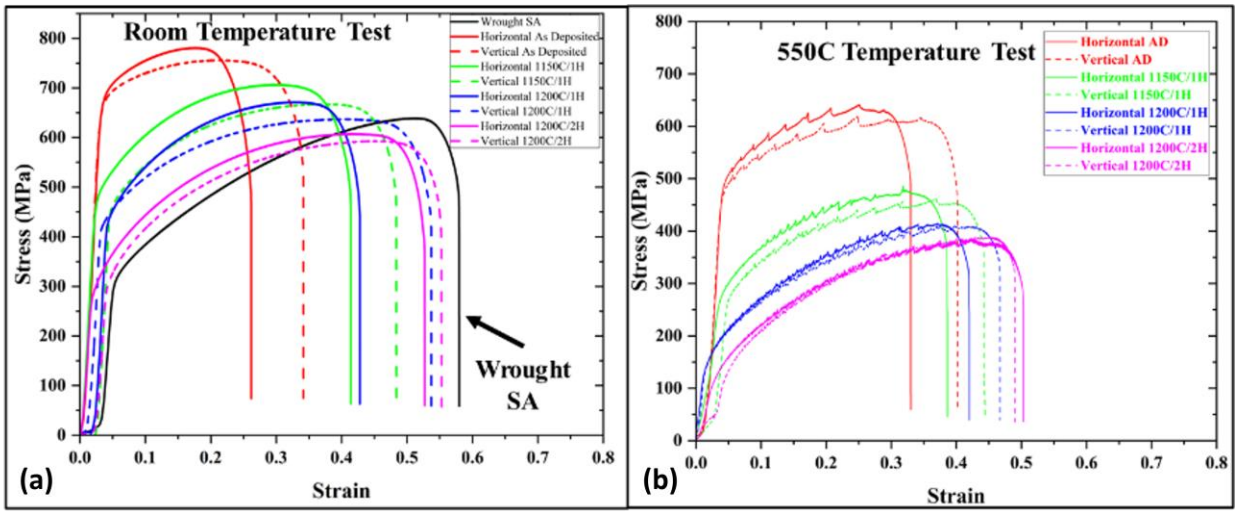

Figure 8. Room and elevated temperature tensile testing of as deposited and solution annealed A709 samples: (a) Room temperature testing, (b) At 550 °C.

A709 was originally developed as a precipitation strengthened alloy. As such, to further explore this, precipitation invoking heat treatments were also done on the alloys (Figure 9). The samples were heated to 775 °C/10H (henceforth called PT) based on the work done by Zhang et al. and Sham et al. (Rupp et al. 2021; Sham et al. 2022). To understand the effect of solution annealing on the subsequent microstructure evolution, the samples solution annealed were also aged at 775 °C/10H. The microstructure of these two conditions is compared to the as deposited and solution annealed samples. As the AD sample and the solution annealed sample have already been discussed in the previous section, this section will focus more on the AD+PT sample and AD+SA+PT. Both conditions show varying amounts of precipitates. These precipitates are observed to be MX carbonitrides and $M_{23}C_6$ carbides. The presence of these precipitates is known to enhance the overall mechanical properties of the alloy for both room and elevated temperatures. As such, room tensile testing was done on these samples and is shown in Figure 10a.

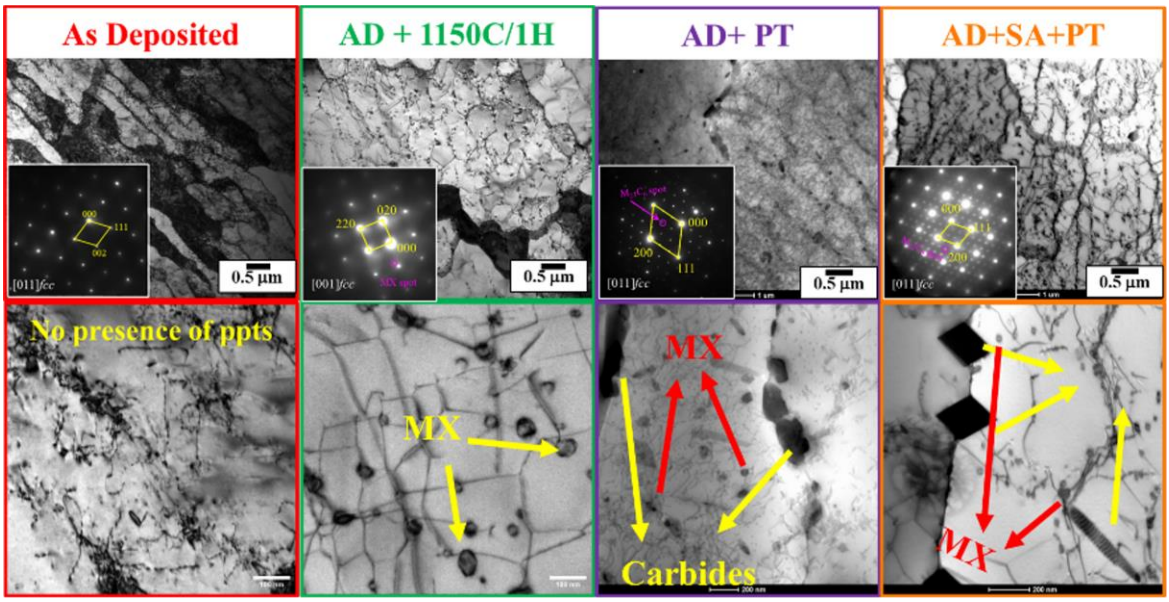

Figure 9. TEM of as-deposited A709 sample compared to the solution annealed, and precipitation treated sample.

The samples which were precipitation hardened showed a big difference in the mechanical behavior, depending on whether a prior solution annealing was done. The AD+PT shows the highest strength among all the samples tested with a yield strength of ~680 MPa and UTS of ~850 MPa. As was seen in the microstructure in the Figure 9, a high number of dislocations + the presence of precipitates ($M_{23}C_6$, MX, θ) can explain the high strength of this condition. In contrast, the sample which was aged after solution annealing had strengths comparable to the just solution annealed sample. The samples were then tested at elevated temperature of 550 °C as shown in Figure 10b. As expected, with an increase in the testing temperature, there is an overall decrease in the yield strength of all the conditions. In the samples tested at 550°C, all the curves exhibited serrated flow during the tensile deformation. Generally, the occurrence of serrated flow has been attributed to the dynamic strain aging (DSA) effect. DSA is caused by the pinning and unpinning of dislocations and solute atoms. In the case of the samples which are deformed at 550 °C, it is likely that the diffusion of substitutional solutes causes DSA. As such it is interesting to notice the change in the “amplitude” and “frequency” of the serrations in the stress-strain curves. The AD sample shows the largest frequency. It should be remembered that the AD sample has no precipitation within the matrix and has the highest amount of segregation of substitution solutes. By aging the sample, we can see that different precipitates are formed in the matrix. For samples subjected to either direct or indirect precipitation, a significant presence of carbide and MX phases is observed in the matrix. The formation of such precipitates will lead to a reduction in solute content within the matrix and thus lower the chances of their interaction with the dislocations. This causes the change in the serrated nature of the curves. The samples with the highest number of precipitates showed the smallest frequency and amplitude.

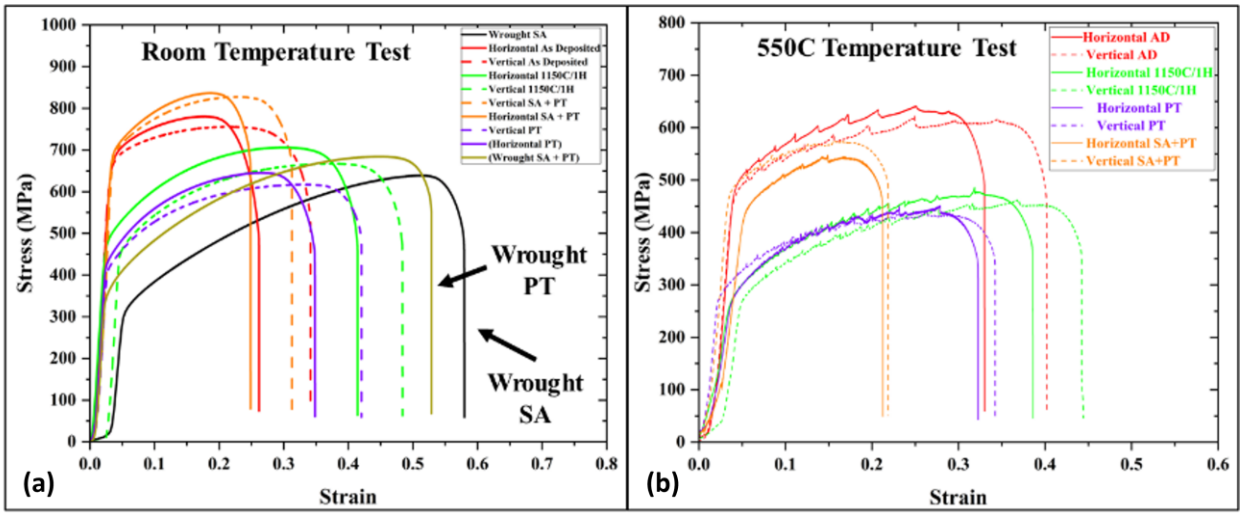

Figure 10. Room and elevated temperature tensile testing of as deposited, solution annealed, and precipitation treated samples: (a) room temperature testing, (b) at 550 °C.

3.2.2 LPBF Ferritic/Martensitic Steel G91

For alloy G91 the standard heat treatments recommended are normalizing and tempering (El-Atwani et al. 2021; Hatakeyama et al. 2023; Klueh and Nelson 2007). These two different heat treatments are performed at 1070 °C /15 min and 770 °C /45 min respectively. As an additional step, we have performed an additional heat treatment that included both treatments. Following normalizing the sample at 1070° C /15 min we tempered the sample at 770 °C /45 min. All these micrographs are put in for comparison and shown in Figure 11. These micrographs are taken along the build direction. The as-deposited samples are shown in the red boxes at different magnifications, 1070 °C /15min in the green boxes, 770 °C/45 min in the turquoise, and the 1070°C /15 min + 770 °C /45 min (two-step) in the blue boxes. All samples were water quenched after the specified heat treatments. Due to the quenching, after holding the sample at 1070 °C, the microstructure appears to be completely transformed into martensite. Martensitic laths can be clearly seen in the high magnification images. No trace of the starting microstructure was found. When the sample was tempered at 770 °C, the original grain structure was retained, but the martensite phase detected along the melt-pools in the as-deposited condition appears to have reduced. The formation of newer phases along the grain boundaries is also noted. Finally, the sample that underwent both treatments exhibits a “tempered” martensitic structure. By aging the sample at 1070 °C, the original microstructure is lost and changes to a martensitic phase. By annealing this sample at 770 °C, tempering of this martensite takes place leading to a “softer” phase. At this scale, we did not notice the presence of any secondary precipitates.

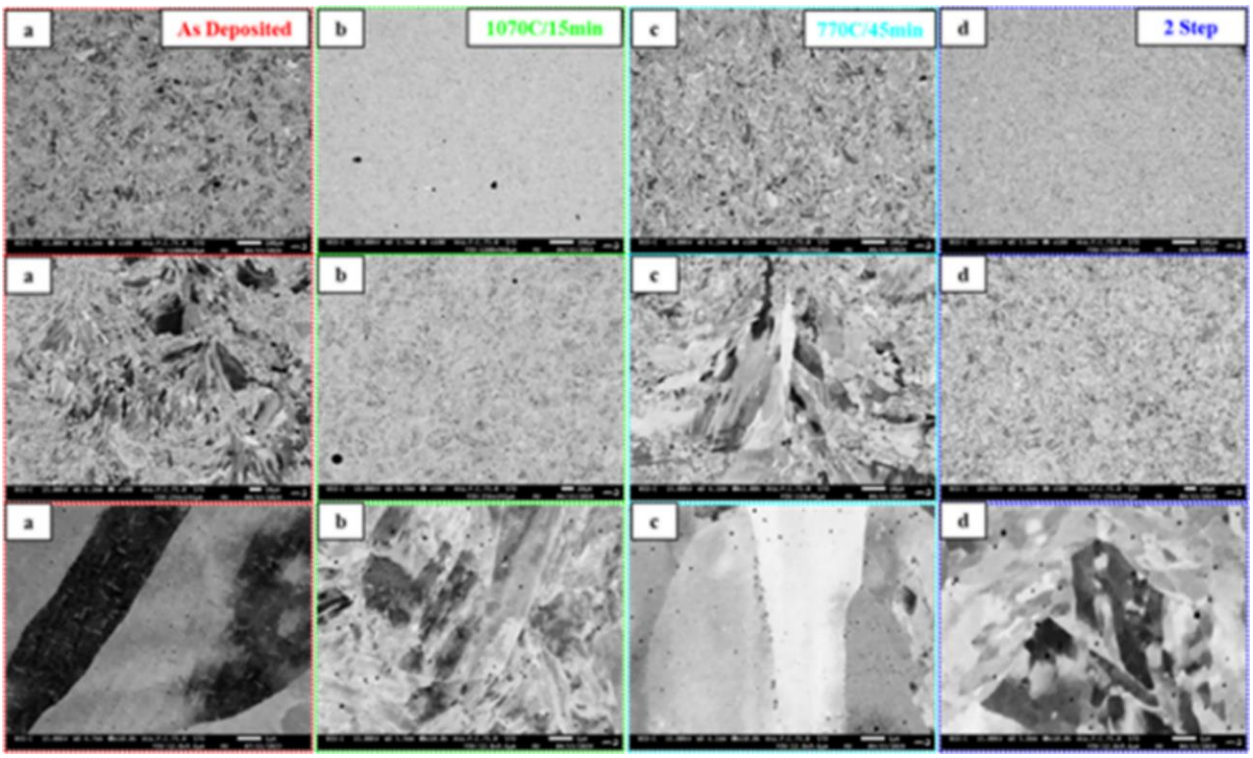

Figure 11. SEM microstructures of additively manufactured G91 after different heat treatments.

Figure 12 show the EBSD IPF maps of all four conditions, both across and along the build directions. In the as-deposited condition, slightly elongated “U-shaped” grains were observed along the build direction. Finer grains were present between the larger grains. Some of the regions were not indexed and are shown as black regions. The “checkerboard” pattern noticed in the IPF maps perpendicular to the build direction is due to the scanning pattern employed during the deposition process. The grains are about ~100 µm in size and have finer grains between the larger grains. Aging the sample at 1070 °C alters the microstructure significantly. The grain sizes from the EBSD analysis were noted to be ~5 and ~10 µm along vertical and horizontal directions respectively. Aging the sample at 770 °C also seemed to have an effect. Tempering of the microstructure leads to dissolution of the martensite phase and indexing was more clearly observed. The overall grain morphology looks very similar to the as-deposited conditions. Finally, the samples which underwent the two-step heat treatments were also analyzed. The EBSD IPF maps are very similar to the samples annealed at 1070 °C. The heat treatment at 770 °C seemed to make no significant difference in this case. To understand the effect of these heat treatments on the mechanical behavior, room temperature tensile tests were performed on these samples and are described in the following section.

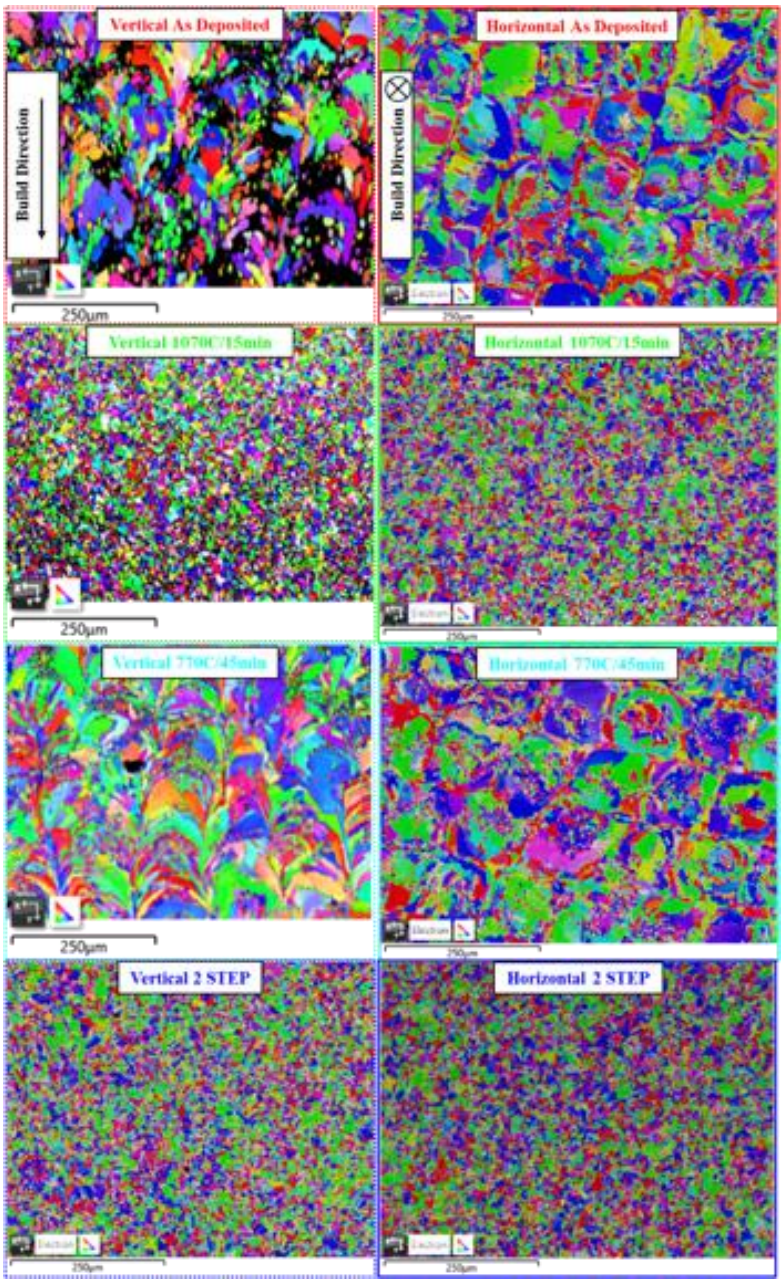

Figure 12. EBSD IPF maps of alloy G91 along and across the build direction after different heat treatments.

The mechanical behavior of these samples is summarized in engineering stress vs strain plot shown in Figure 13. The as-deposited samples show a good combination of strength and ductility with UTS reaching around 900MPa and strain to failure around 20%. The samples aged at 1070 °C showed the highest strength with UTS around 1300 MPa. This is to be expected as the microstructure is solely made up of martensite. The samples which underwent the 770 °C heat treatment, with and without the 1070 °C treatment, had the lowest values of strength with values around 600 MPa. Further work is being doing to test these samples at elevated temperatures and to study the deformation behavior.

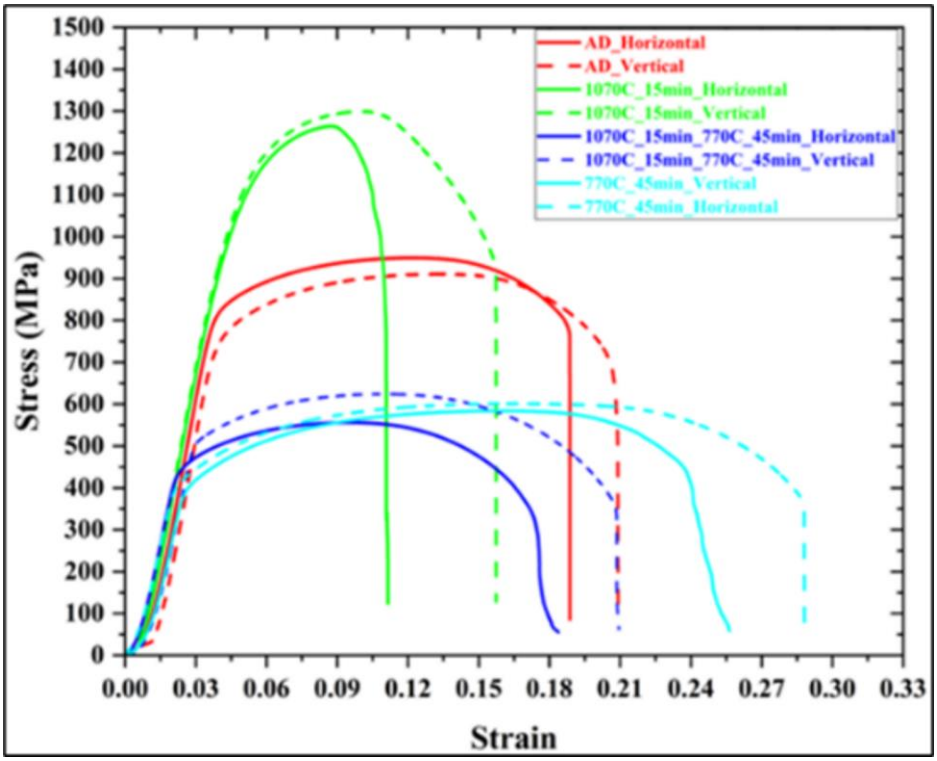

Figure 13. Room temperature mechanical behavior of additively manufactured G91 after different heat treatments.

3.2.3 LPBF Ferritic/Martensitic Steel G92

Similar to G91, after the deposition, the alloy was subject to three different heat treatments. These are shown in Figure 14 at different magnifications. The as-deposited sample has a mixture of bcc phase along with some secondary precipitates, possibly thought to be carbides along the grain boundaries. Upon aging the sample at 1070 °C/15 min, the microstructure completely transforms to martensite. The tempering heat treatments (both with and without the prior aging) are similar to what was noticed in G91. The single step retains the microstructure similar to the as deposited one, while the sample with prior aging looks like the sample aged at 1070 °C, i.e. martensite.

The addition of W leads to an overall increase in the strength of these alloys. This is reflected in the room temperature tensile behavior, shown in Figure 15. The as deposited sample has UTS around 1100MPa with a strain to failure around 12%. Annealing the sample at 1070 °C leads to a massive increase in the UTS to ~1500 MPa. Like alloy G91, the tempering treatment leads to lower strengths, but improved ductility. More work needs to be done to understand the mechanical behavior of this alloy and will be pursued in the upcoming FY25.

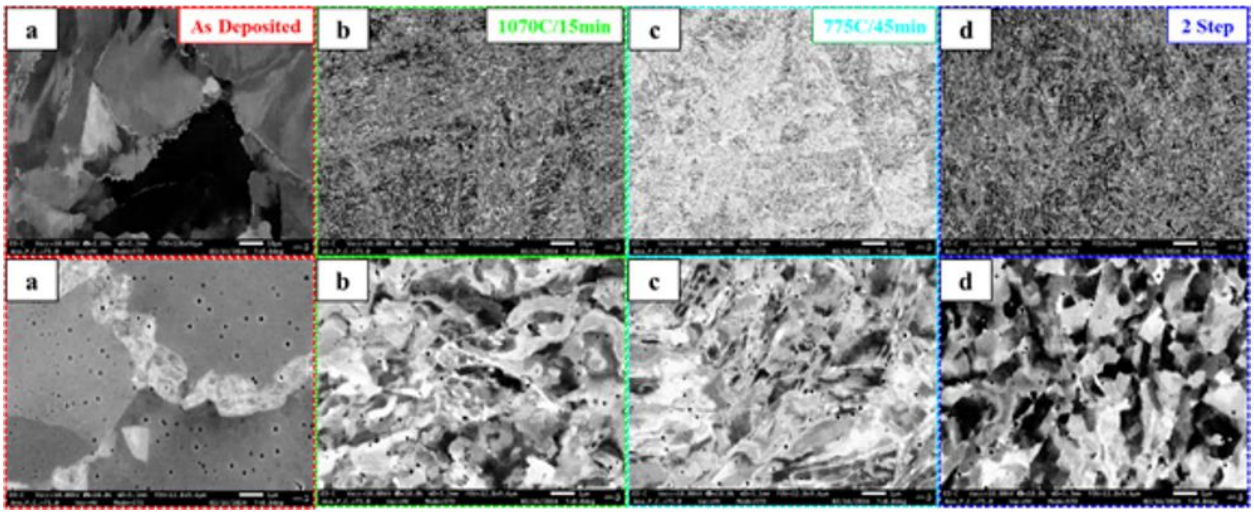

Figure 14. SEM images of G92 alloy after heat treatments.

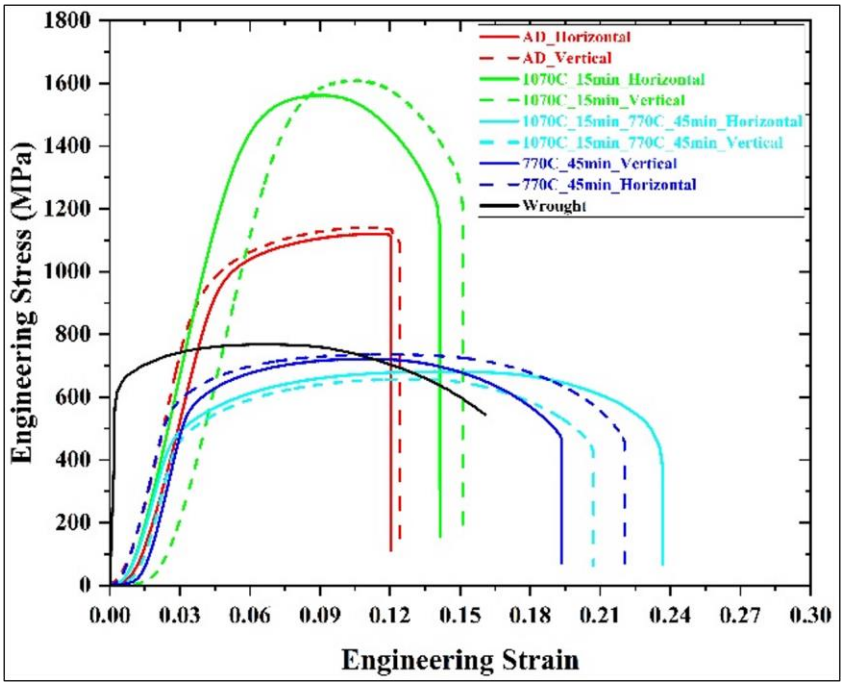

Figure 15. Room temperature mechanical behavior of the alloy G92 after different heat treatments.

3.3 LP-DED of A709, G91 and G92 Steels

Previous work emphasized on the preliminary microstructural and mechanical property of alumina forming austenitic alloys HT-9, D-9, FeCrAl ODS, and Grade-91 produced by LPBF (Meher et al. 2023). In this section, results from a printability study of laser directed energy deposition (DED)-based additive manufacturing of nuclear-grade stainless steels as well as DED process parameter development for austenitic Alloy A709 and ferritic/martensitic G91 and G92 steels will be presented (Meher et al. 2024). In the DED process development work, 1 cm^3

alloy blocks were deposited with broad ranges of laser powers, scan speeds, and hatch spacings to optimize the build quality, resulting in densities of more than 99.8% for all three alloys. The microstructure and mechanical properties were characterized using electron microscopy, X-ray diffraction, and Vickers hardness measurements. Further, tensile samples were extracted from DED-fabricated alloys utilizing the optimized process parameters.

The results from each alloy fabricated by powder DED are presented here. To be consistent with the LPBF results of each of the alloys, the SEM/EBSD microstructure of the as-deposited sample and the Vickers's hardness will be presented here. As the development work on the DED printability of these alloys commenced only in FY24, the results presented here are preliminary and not yet fully developed; comprehensive interpretation is ongoing. Based on the literature data and discussion by Meher et al. (2024), it was determined that the optimal process parameter overlapped for the three alloys. The average laser powers and scan speeds in related to G91 and G92 steels correlate with the low laser powers and scan speeds in related to Type A709 steel. As such, a single range of process parameters was selected for the first parameter window evaluation with all three alloys. The selected experimental envelope is presented in Table 3.

Table 3. DED process parameter matrix to be used for all three alloys.

Laser Power, W	Laser Scan Speed, mm/min
400, 500, 600, 700	500, 600, 700, 800

3.3.1 LP-DED Austenitic Steel A709

LP-DED process parameter literature study showed that A709 may be proned to hot cracking at higher laser powers (Meher et al., 2024). Because of the potential for hot cracking susceptibility of Type A709 steel, special consideration included using a lower laser power than compared to the wide range of laser powers for 300-series steels would reduce the thermal gradient and cooling rate, which in turn decreases the risk of hot cracking during DED fabrication through increased uniformity in cooling and solidification of the specimens. Meanwhile, decreasing the scan speed relative to the range of values reported in the literature study by Meher et al. 2024 also reduces hot cracking susceptibility through more uniform solidifcation. As a verificiation, A709 samples produced with various laser powers and scan speeds were analyzed. The samples had porosities of 0.03%–1.1%; however, cracks were observed in some samples; especially the higher laser power as expected. It was observed that a lower laser power produced denser products. Hence, tensile samples were fabricated with a laser power of 400 W and a scan speed of 600 mm/min, which was observed to be fully dense (99.97%). Figure 16 presents the variation in the Vickers hardness with the change in the laser power while the laser scan speed was kept constant. It was observed that in general, the Vickers hardness tended to decrease as the laser power increased when the laser scan speed was kept constant. This could potentially be attributed to the increase in grain size due to the higher laser power input.

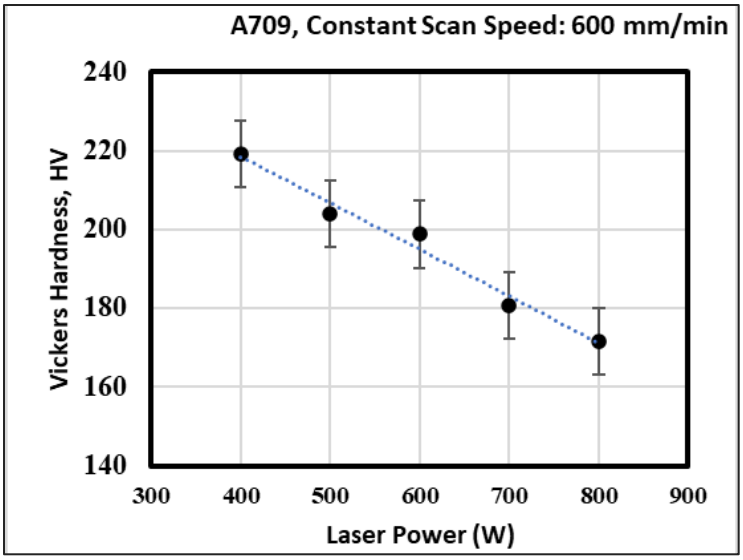

Figure 16. Variation in the Vickers hardness with the laser power at a constant scan speed for A709 steel.

The A709 sample fabricated with a laser power of 400 W and a scan speed of 600 mm/min showed the highest density. In general, the porosity was 0.03%–1.1%; however, few cracks were observed in some samples. The microstructure of austenitic A709 steel primarily consisted of a cellular dendritic structure decorated within the elongated grains. The XRD pattern revealed the presence of the austenitic FCC phase. Figure 17 presents representative backscattered electron micrographs of austenitic A709 steel at different magnifications. The microstructure primarily consists of elongated grains with a cellular dendritic structure decorated within the grains. Representative EBSD orientation maps of austenitic A709 steel are presented in Figure 18. The average Vickers hardness determined from the fully dense sample was observed to be 219.27 ± 7.79 HV.

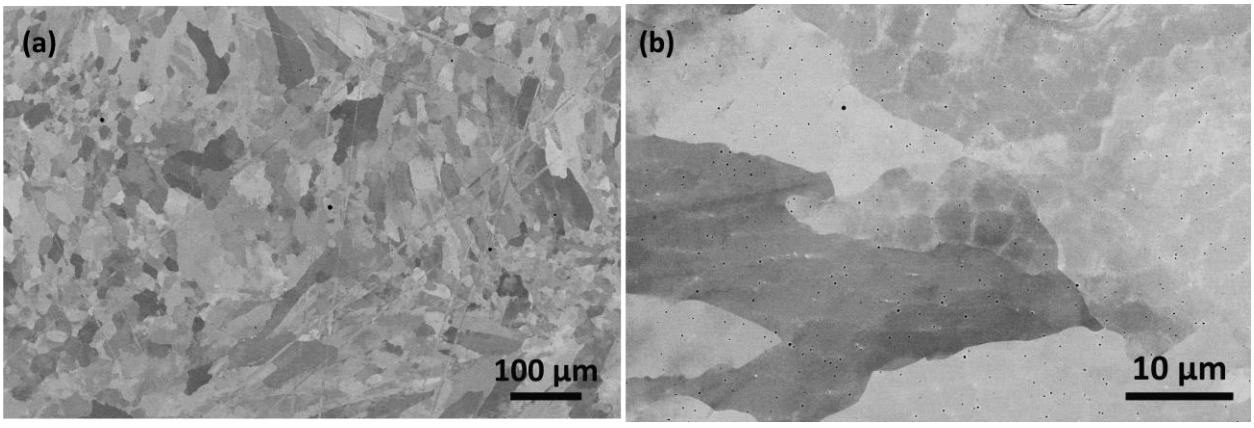

Figure 17. Representative backscattered electron micrographs of austenitic A709 steel: (a) low magnification and (b) high magnification depicting the dendritic cellular structure.

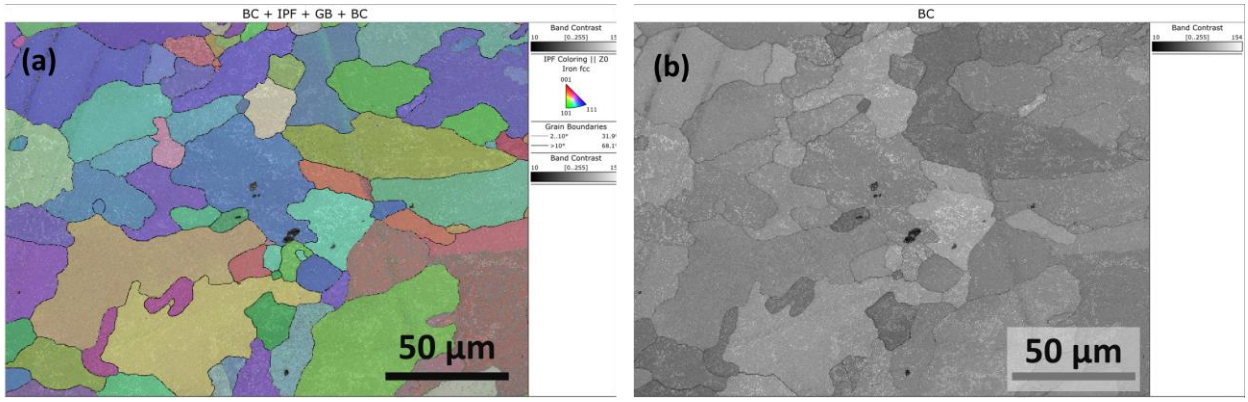

Figure 18. Representative EBSD orientation maps of austenitic A709 steel: (a) inverse pole figure and grain boundary contrast and (b) band contrast.

3.3.2 LP-DED Ferritic/Martensitic Steel G91

AM of Grade 91 and Grade 92 F/M stainless steels has mainly utilized LPBF in past research. The limited publications on DED of F/M steels and the associated process parameters are outlined in Meher et al., 2024. While no work has been found on DED of G92 steel, G91 is expected to be nearly identical in both performance and fabrication (Lienert and Maloy 2017). As such, it was determined that identical DED process parameters would be used for both G91 and G92 steels.

Of primary concern in the realm of F/M steels is the martensite start (M_s) temperature, which is controlled primarily by the Mn content, along with the Cr, Mo, Si, and C contents, where increased contents of these elements can decrease the M_s temperature. A high M_s temperature increases tensile residual stresses, which in turn increases the brittleness of the alloy (Zhong et al. 2021). Brittleness is of great concern during fabrication with DED processes due to the large thermal gradients and rapid cooling and solidification during fabrication. An aspect of the methodology for process parameter selection was a qualitative comparison of the above elements to determine whether M_s was improved compared to the relevant publications. Compared to Fe–9Cr (Whitt et al. 2023) and Fe–9Cr–2W–V (Gräning and Sridharan 2022), G91 and G92 steels have higher contents of most of the elements that lower the M_s temperature, and as such, the two latter alloys are likely less brittle than the two former alloys for the same process parameters. However, the literature provided evidence of other alloys with similar compositions to those of the G91 and G92 steels of successful DED printed products.

The experimental work performed as part of the AMMT program showed that the G91 sample fabricated with a laser power of 500 W and a scan speed of 600 mm/min and a hatch spacing of 0.9 mm showed the highest density. The porosity was observed to be 0.03%–3.62%. The XRD pattern indicated strong reflections from BCC α-ferrite. It is assumed that the peaks corresponding to BCC ferrite and body-centered tetragonal (BCT) martensite overlapped because of broadening. The microstructure of G91 steel primarily consisted of fine and coarsened lath martensite. The average Vickers hardness determined from the fully dense sample was observed to be 398.08 ± 17.16 HV. Figure 19 presents the variation in the Vickers hardness with the change in the laser power while the laser scan speed was kept constant for the G91 samples. It was observed that in general, the Vickers hardness tended to decrease as the laser power increased when the laser scan speed was kept constant. This could potentially be attributed to the increase in grain size due to higher laser power input.

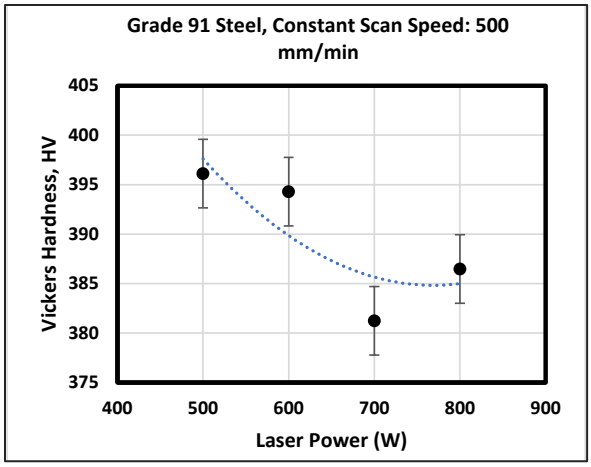

Figure 19. Variation in the Vickers hardness with the laser power at a constant scan speed for F/M Grade 91 steel.

Figure 20 shows representative backscattered electron micrographs of G91 steel at different magnifications. The microstructure primarily consists of fine and coarsened lath martensite. Representative EBSD orientation maps of G91 steel are presented in Figure 21.

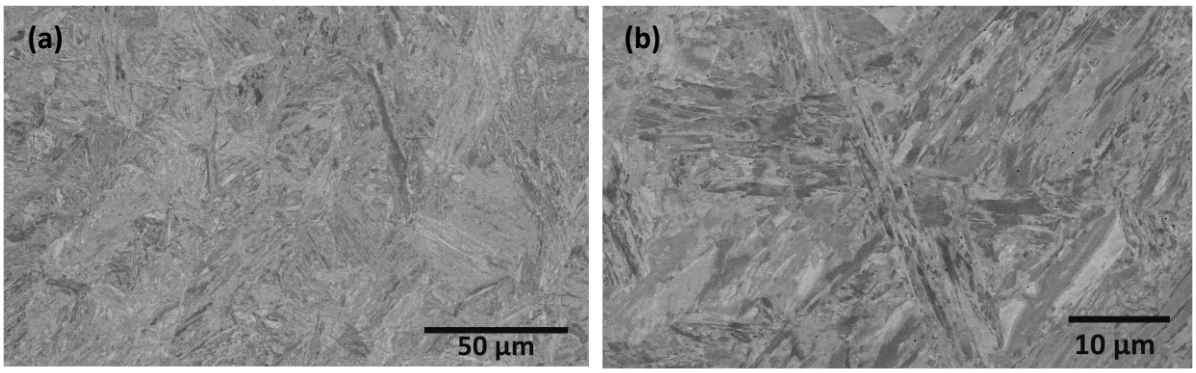

Figure 20. Representative backscattered electron micrographs of G91 steel: (a) low magnification and (b) high magnification.

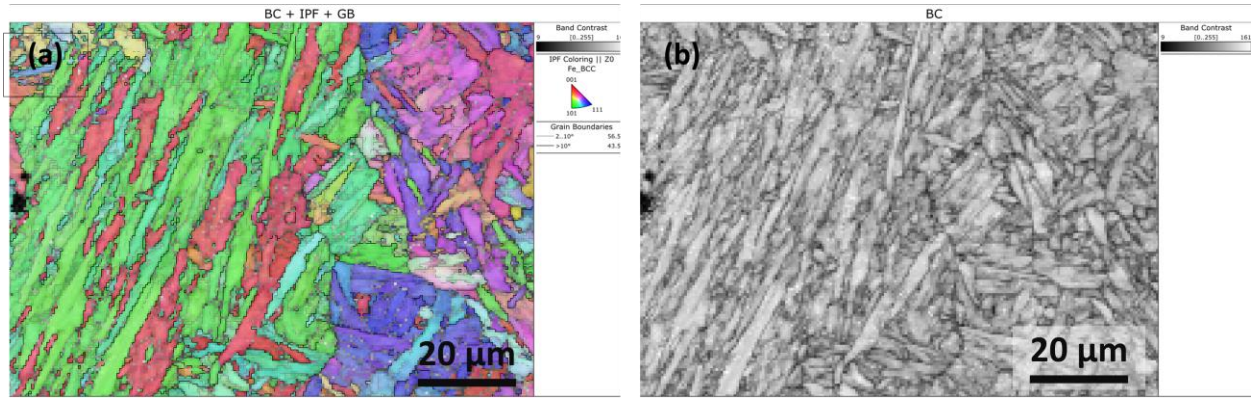

Figure 21. Representative EBSD orientation maps of G91 steel: (a) inverse pole figure and grain boundary contrast and (b) band contrast.

3.3.3 LP-DED Ferritic/Martensitic Steel G92

The G92 sample fabricated with a laser power of 500 W and a scan speed of 700 mm/min showed the highest density. The porosity was observed to be 0.15%–2.53%. Like the G91 steel, the XRD pattern indicated strong reflections from BCC α-ferrite, and the peaks corresponding to a BCT martensite phase are assumed to be buried under the BCC peaks. The microstructure of G92 steel primarily consisted of fine and coarsened lath martensite. The average Vickers hardness determined from the fully dense sample was observed to be 432.05 ± 23.05 HV. Figure 22 presents the variation in the Vickers hardness with the change in the laser power while the laser scan speed was kept constant. Like G91 steel, it was observed that in general, the Vickers hardness tended to decrease as the laser power increased when the laser scan speed was kept constant, which could potentially be due to the increase grain size at a higher laser power. Figure 23 shows representative backscattered electron micrographs of G92 steel at different magnifications. The microstructure primarily consists of fine and coarsened lath martensite. Representative EBSD orientation maps of G92 steel are presented in Figure 24.

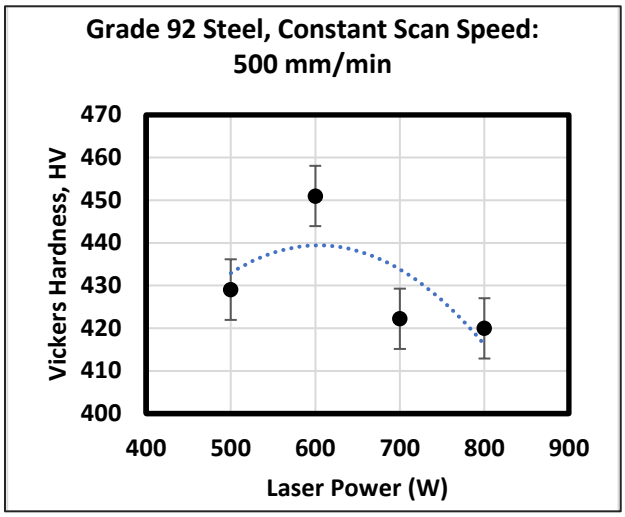

Figure 22. Variation in the Vickers hardness with the laser power at a constant scan speed for F/M Grade 92 steel.

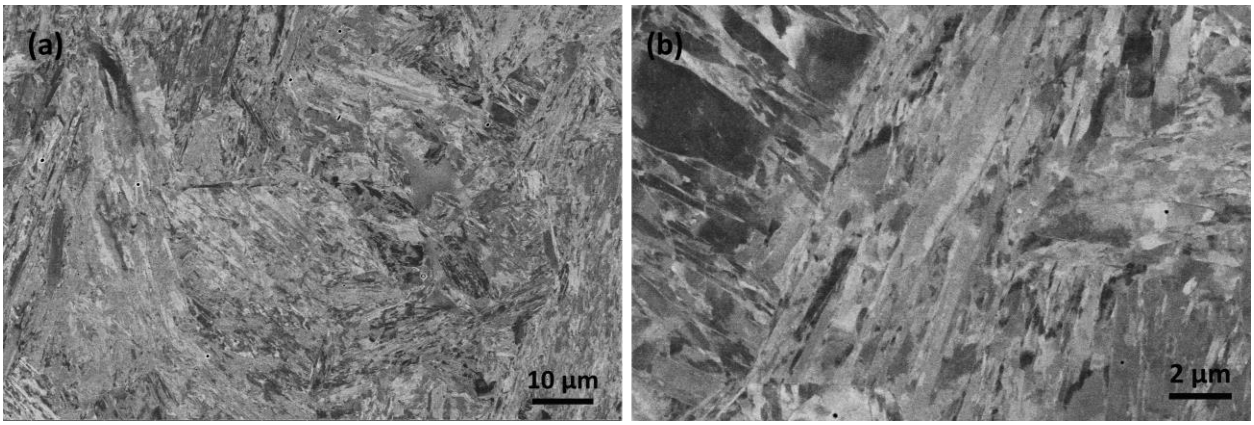

Figure 23. Representative backscattered electron micrographs of G92 steel: (a) low magnification and (b) high magnification.

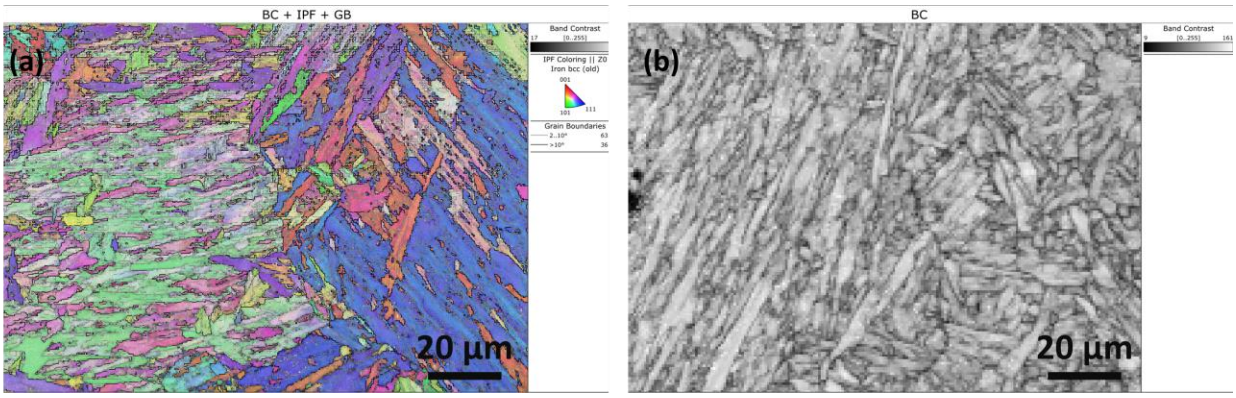

Figure 24. Representative EBSD orientation maps of G92 steel: (a) inverse pole figure and (b) band contrast.

3.3.4 Summary of LP-DED A709, G91 and G92 Development

LP-DED printing parameters were successful determined for all three alloys investigated and hot cracking was less of a challenge than theoretically expected. Figure 25 shows the fabricated cubes of (a) A709, (b) Grade 91, and (c) Grade 92 steels and tensile samples of (d) A709, (e) Grade 91, and (f) Grade 92 steels. The tensile properties will be determined in FY25 as well as heat treatment trials.

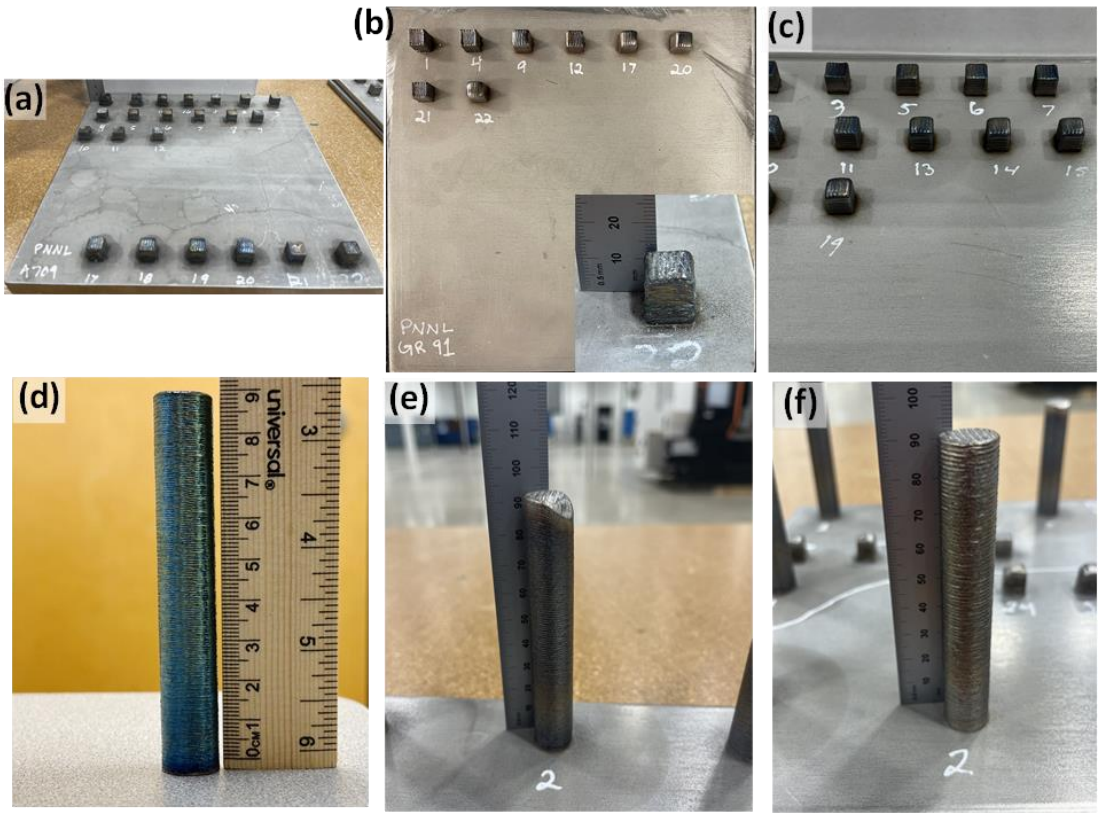

Figure 25. Fabricated cubes of (a) A709, (b) Grade 91, and (c) Grade 92 steels and tensile samples of (d) A709, (e) Grade 91, and (f) Grade 92 steels.

Main conclusions are as follows:

- The A709 sample fabricated with a laser power of 400 W and a scan speed of 600 mm/min showed the highest density. In general, the porosity was 0.03%–1.1%; however, a few cracks were observed in some samples. The microstructure of austenitic A709 steel primarily consisted of a cellular dendritic structure decorated within the elongated grains. The XRD pattern revealed the presence of the austenitic FCC phase. The average Vickers hardness determined from the fully dense sample was observed to be 219.27 ± 7.79 HV.
- The G91 sample fabricated with a laser power of 500 W and a scan speed of 600 mm/min showed the highest density. The porosity was observed to be 0.03%–3.62%. The XRD pattern indicated strong reflections from BCC α-ferrite. It is assumed that the peaks corresponding to BCC ferrite and body-centered tetragonal (BCT) martensite overlapped because of broadening. The microstructure of G91 steel primarily consisted of fine and coarsened lath martensite. The average Vickers hardness determined from the fully dense sample was observed to be 398.08 ± 17.16 HV.
- The G92 sample fabricated with a laser power of 500 W and a scan speed of 700 mm/min showed the highest density. The porosity was observed to be 0.15%–2.53%. Like the G91 steel, the XRD pattern indicated strong reflections from BCC α-ferrite, and the peaks corresponding to a BCT martensite phase are assumed to be buried under the BCC peaks. The microstructure of G92 steel primarily consisted of fine and coarsened lath martensite. The average Vickers hardness determined from the fully dense sample was observed to be 432.05 ± 23.05 HV.
- As-fabricated hardnesses corresponding well with prior literature of similar alloys. Table 4 presents a summary of the Vickers hardness observed for all three alloys along with the Vickers hardness values of similar steels reported in the literature.

Table 4. Summary of the Vickers hardness of A709, G91 and G92 as compared with other austenitic and ferritic/martensitic steels.

Category	Alloys	Fabrication Technique	Vickers Hardness	Ref.
Austenitic steels	SS304	AM-LPBF	254 ± 7.00	(Hartmann et al. 2022)
	A709	AM-DED	219.27 ± 7.79	This study
	D-9	LPBF	189.3 ± 16.8	(Meher et al. 2023)
Ferritic/Martensitic steels	Grade 91	AM-DED	398.08 ± 17.16	This study
	Grade 91	AM-Wire Arc	412 ± 23.04	(Robin et al. 2024)
	Grade 91	LPBF	281.4 ± 21.1	(Meher et al. 2023)
	HT-9	LPBF	411.6 ± 24.7	(Meher et al. 2023)
	Grade 92	AM-DED	432.05 ± 23.05	This study

3.4 Chemical Composition-Based Machine Learning and Multi-physics Model to Predict Defect Formation in Additive Manufacturing

AM holds immense promise for producing components with complex geometries, making it a valuable technology in industries like nuclear engineering. However, defects such as porosity, balling, and lack of fusion pose significant challenges, impacting the mechanical integrity of parts. This study integrates machine learning (ML) techniques with Flow-3D simulations to predict and understand defect formation in additively manufactured components. The aim is to identify optimal process parameters and alloy compositions that minimize defects, improving the reliability and performance of AM components for critical applications (more details provided in Meher et al., 2024. Roy et al., 2024).

3.4.1 Results and Discussion

Three machine learning models—random forest (RF), gradient boosting regressor (GBR), and neural network (NN)—were developed to predict the likelihood of defects based on AM process parameters and alloy compositions. The models were trained on a dataset that included both traditional alloys and high-entropy alloys (HEAs). The performance of the 3 models is shown by the prediction accuracy in Table 5. The NN is the most accurate model of the three (highlighted in Table 5) for the balling data sets and accuracy increases when both traditional alloys and HEAs are combined in the balling training set. The RF regressor is the most accurate model for the porosity data.

Table 5. Prediction accuracy of the 3 models using the 2 datasets.

Model	Accuracy with balling dataset 1 (No HEAs) (%)	Accuracy with balling dataset 2 (with HEAs) (%)	Porosity R^2 score	Mean Squared Error (MSE)	Root Mean Squared Error (RMSE)	Mean Absolute Error (MAE)
RF Classifier	69.2	73.1	NA	NA	NA	NA
RF Regressor	NA	NA	0.971	0.0119	0.109	0.0518
GBR	84.6	88.5	0.955	0.0184	0.1357	0.0739
NN	88.5	92.3	0.0221	0.421	0.649	0.343

When the NN model trained on both datasets, it is seen that along with the process parameters (laser power and scan speed) some chemical features, like Cu, Si, S, Fe, W and Nb seem to be significantly impacting balling. When the NN was trained on dataset 1 (without the HEAs), Cu, Si, C, S and Fe were indicated as some of the most significant chemical descriptors. The connection to the laser power can be seen as sufficient melting of the powder, while high scan speeds mean the opposite, i.e., insufficient melting (Chen et al. 2017). When the NN was trained on dataset 2 (includes HEAs), C and S remained as some of the most significant ones, but the W and Nb occupied the following ranks, due to the inclusion of HEAs. Dataset 1 had around 40 datapoints with steel and 20 datapoints with Inconel 718 that were the major alloys

containing carbon. Despite the differences in the nature of the training dataset, C and S seem to be consistently impacting the occurrence of balling.

To systematically investigate the influence of carbon content on the printability of stainless steels, a targeted system was selected for multiphysics simulations using FLOW-3D. These simulations were conducted through a collaborative effort between Pacific Northwest National Laboratory (PNNL) and Oregon State University (OSU), focusing on Directed Energy Deposition (DED) processes applied to SS 316L and SS 316H. To run the simulation model for SS 316L and SS 316H, it was imperative to incorporate precise temperature-dependent properties such as thermal conductivity, specific heat capacity, density, viscosity, and surface tension, along with non-temperature-dependent properties like liquidus and solidus temperatures and latent heat of fusion. These critical thermophysical properties for SS 316L and SS 316H were meticulously obtained through Thermo-Calc software, leveraging PNNL's licensed access to the database. Utilizing this enhanced material dataset, OSU initiated trial simulations by modifying an existing SS 304 template within FLOW-3D to accommodate the specific properties of SS 316L and SS 316H. Preliminary results from these simulations are depicted in Figure 26.

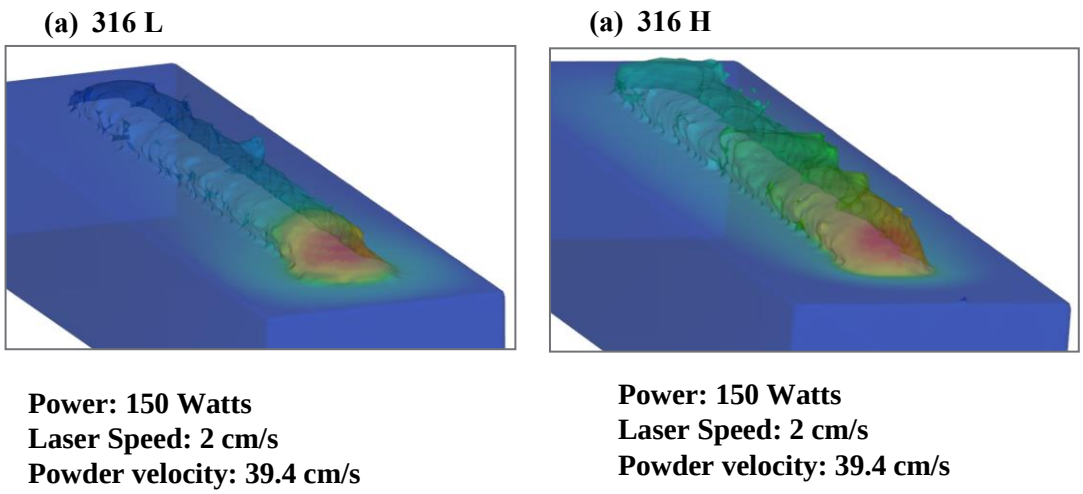

Figure 26. Trial simulations conducted by OSU utilizing the accurate material properties of (a) SS 316 L and (b) SS 316 H. The simulations were performed using identical process parameters for both materials, as indicated in the figure. Qualitative analysis of the printed tracks suggests that SS 316 L produced a more uniform and visually superior track compared to SS 316 H.

PNNL is currently acquiring the Flow 3D license to independently complete the proposed simulations. The primary goal over the next six months will be to train on and utilize the software to fulfill the project objectives and conduct a comparative study of SS 316 L and H.

3.4.2 Conclusions

In summary, a chemical composition-based ML model is proposed, for predicting the tendency of balling defect formation and porosity percentage in alloys during additive manufacturing using a laser-based method. The dataset was curated from literature that included traditional alloys and HEAs with a total of 267 data points describing balling defect formation at various

processing conditions in these alloys, and 138 data points describing porosity percentage at various processing parameters, along with element specific properties. 3 models, RF classifier, GB regressor and a neural network were trained on 2 datasets (dataset 1: excluded HEAs and dataset 2: included HEAs) and their accuracies were calculated from the testing data. The NN model trained on dataset 2 proved to be the most accurate in predicting balling defect formation with an accuracy of 92.3%. 2 models, RF regressor and GB regressor were trained on the porosity dataset. The RF regressor was the most effective at predicting the percent porosity with the lowest MSE of 0.0119. These models revealed that along with the processing conditions such as laser power and scan speed, silicon and carbon significantly impact the tendency to form balling defects, while thermal conductivity and carbon were significant factors in porosity. The inclusion of steel data in the training set led to the identification of carbon as a significant contributor to both types of defects. These findings are in line with metallurgical principles as it is known that small amounts of carbon can highly alter the solidification and deformation properties of steel, thus serving as an initial validation of the models. In conclusion, the collaborative simulations conducted using ML and FLOW-3D have provided valuable insights into the impact of alloy composition, particularly carbon content, on the printability of SS 316L and SS 316H during AM processes. The findings underscore the importance of tailored compositional adjustments in optimizing process outcomes and pave the way for further refinement of additive manufacturing processes through data-driven, multiphysics modeling. The findings have been recently published in (Roy et al. 2024).

4.0 Business Value Considerations

A brief preliminary overview is given on some of the business value consideration that will need to be given for deployment of these AM techniques and decision-making regarding choices of the type of product-AM technique combination.

4.1 Process Economics

AM offers engineers the ability to manufacture complex geometry, often referred to as "complexity is free." However, this complexity comes at a cost like increased build time, potential build failures, and essential post-processing of the produced complex geometry. Costs such as feedstock usage are related with build time. Therefore, optimization of design while meeting design specifications might help reduce overall costs (Song et al. 2020). Few reports indicate wide variances in costs based on machine usage, maintenance, operational costs, and feedstock, making direct cost comparisons difficult due to factors like part geometry and alloy composition (Busachi et al. 2017; Gisario et al. 2019).

The cost of powder feedstock typically varies depending on the alloy. Commercially available alloy powders are readily available and is comparatively cheaper, however, custom alloy powders are generally expensive due to special processing requirements. Cost generally varies depending on different AM processes because of setup, programming, and post-processing operations. For example, aerospace components, specifically, require detailed documentation and traceability, increasing setup costs (Gradl et al. 2022). Similarly, this will be the case for components produced for nuclear reactors. It is reported that 70 % of the total part cost can be attributed to the pre and post-processing operations which includes steps like powder removal, support removal, build plate removal, materials characterization, mechanical testing and heat treatment (Tavcar and Nordin 2021).

Despite some economies of scale and learning curves, the unit costs in AM do not change much with increased build quantities (Dicknes and Hopkinson 2003; Thomas and Gilbert 2014). While some literature suggests that AM-based prototyping might lead to significant cost reduction, while some reported that is not as good as conventional manufacturing in terms of return of investment (ROI) (Niaki et al. 2019) but the feasibility heavily depends on part size, material, and complexity. In some cases, AM might potentially be the only way to manufacture certain parts and allows for high volume production (Herzog et al. 2016). The primary process cost in AM is based on the material being built or deposited. With the increase in overall part volume, the cost increases, however this is primarily dependent on deposition rate. With the increase in deposition rate, the cost can be minimized, at the expense of feature resolution and complexity. This is where processes like DED, cold spray, and additive friction stir deposition have certain advantages compared to LPBF. With the high deposition rate, the complexity of features decreases, and extra stock must be machined away for critical mating surfaces, holes, flanges, and key features which increases the overall cost. Thus, the optimal manufacturing path should be determined via detailed evaluation of the entire AM process life and post processing required (Gradl et al. 2022).

4.2 Supply Chain Risks

The Gateway for Accelerated Innovation in Nuclear (GAIN) conducted a survey to evaluate the current and potential capabilities of supply chains for advanced reactor components focusing on sodium, gas-cooled, and molten salt reactors. Using an aggressive nuclear deployment

scenario, the survey aimed to assess the supply chains' ability to meet high demand projections for key components like vessels, heat exchangers, pumps, graphite, and sensors, and to identify potential challenges. Although individual companies struggled to meet the most optimistic deployment rates, the survey showed that United States-based supply chain could potentially be expanded to meet future demand. However, fulfilling demand for more complex items such as gas or salt heat exchangers will potentially be a challenging task. U.S. suppliers believe they can meet the future demand for advanced reactor components if appropriate investments are made in the supply chain sooner. Meeting the 5-10-years production targets will require immediate investment. For significant nuclear deployment in the 2030 and beyond, ramping up the advanced nuclear supply chain needs to start soon to ensure the United States can deploy these reactors using domestic resources (Lohse et al. 2023). Advanced manufacturing method could potentially come handy for alternative supply chains for some nuclear components, however large-scale manufacturing and its successful rapid qualification are some of the challenges involved that needs to be addressed. In addition, creating a skilled workforce should be given a priority (Shingledecker et al. 2022).

When considering new alloy systems for additive manufacturing, one of the major roadblocks is powder procurement (Mantri and Zhang 2023). Most of the alloys currently used or being explored are available in wrought or cast forms. Unfortunately, that is not the case for the powder and not all powders are readily available off-the-shelf. While using customized powders is an option, these usually have a minimum quantity requirement and a very long lead time. Even if the powder is obtained, there are multiple other factors which need to be explored/understood (Dawes et al. 2015). In DED process, the alloy powder is fed coaxially with the laser beam by a set of nozzles. A carrier gas is used to transport the gas into the nozzles and onto the melt pool. In contrast for an LPBF process, the part forms by spreading of thin layers of powders followed by laser raster. As such, the LPBF techniques often use powder sizes within the range of 10-45 microns while the DED requires larger sizes, in the range of 50-200 microns (Sames et al. 2016). The main trade-off in the selection of powder size is cost vs. surface finish. Smaller particles tend to improve surface finish due to reduction of the size of satellites. However, smaller powder particles may cost more as a feedstock (than a larger size range) due to lower yields for smaller particles in powder production (depends on production technique). The other factor to consider includes the powder chemistry. The high cooling rates in AM builds lead to specific non-equilibrium microstructure and variation of the alloy chemistry within the alloy specification and may have an impact on the alloy microstructure and properties (DebRoy et al. 2018). The cost of powder is a very important criterion which needs to be taken into consideration as most of the customized powders could lead to higher costs. The recyclability of the powders also goes hand-in-hand with the cost of the powders. Alloy powders which can be recycled and reused will lower the overall cost (Thomas 2016).

4.2.1 Supply Chain for Both LPBF and LP-DED for the Three Alloys Investigated

As mentioned in an earlier section, most of the alloy powders currently used or being explored for nuclear applications are not readily available off-the-shelf. While using customized powders is an option, these usually have a minimum quantity requirement and a very long lead time. For the current work, the three alloys being explored, A709, G91, and G92 fall into this category. For FY23, as the work was exploratory, 15 kilograms of each alloy was sufficient to do the initial printing (using the reduced build volume chamber in Renishaw 400AM machine). As the alloys were still custom made, the overall cost was more than $40,000 for all the three alloys, meaning about ~$1000 per kilogram. To put this in context, single kilogram of SS316 costs somewhere between $60-100. These powders were obtained from Atlantic Equipment Engineers and had a

lead time of approximately ~ 4 weeks. For FY24, once the process parameters were optimized, we needed larger quantities of powders, i.e. >100 kgs., to build larger parts. As such, 100 kgs of each alloy was provided by Praxair Inc (now Linde Inc). For FY 24, other than LPBF, as DED work was also being done on these alloys, a different size of the same powders was also required. When the alloys are made into powder (by atomization or any other technique), they are then sieved to the required sizes as needed by the customer/user. As Praxair was already making the powders for us in the sizes required for LPBF, it was easy to obtain the powders for DED. This also helps reduce not only the overall costs for the customers, but also prevents wastage (other sizes of powders are usually discarded). Overall, we were able to get 100 kgs of LPBF powder and 40 kgs of DED powder. It should be noted that the price of the DED powder was lower than the price of LPBF powders, i.e. $320 to $120 for A709, $300 to $120 for Grade-91 and Grade-92. Considering Praxair is one of the leading companies currently in the powder manufacturing business, the caveat is the long lead times. To get the 140 kgs of each alloy, the overall lead time was 12-16 weeks. This might lead to a significant delay in the overall process when considering supply chain. Both the suppliers used for the current work are based in USA.

4.3 Reactor-Specific Targeted Components

DED has the capability of producing site specific components on the size scale of meters as shown in Figure 3, for example, valves, pumps, and impellers that are sometimes difficult to source when developing a new system or replacing obsolete components (Nag et al. 2023). This advantage of DED can be utilized to fabricate reactor specific components in critical times. The primary objective of the US DOE-NE Transformational Challenge Reactor (TCR) program is to reduce the deployment costs of new nuclear power generation. This can potentially be achieved by advancements across various disciplines via speeding up the design, manufacturing, qualification, and deployment processes for advanced nuclear energy systems. This approach can be enabled by the use of AM technologies and the adoption of key agile development principles (Betzler et al. 2020).

Debris fretting, caused by debris-induced wear on fuel rod cladding, is the primary cause of leaks in pressurized water reactor (PWR) fuel assemblies. The debris filtering capabilities can potentially be enhanced by allowing for more sophisticated designs via AM that minimize the size of debris entering the reactor. Westinghouse Electric Company utilized additive manufacturing (AM) to create bottom nozzles designed to enhance debris capture and fuel longevity in its fuel assemblies. These nozzles were incorporated into four Lead Test Assemblies, which were delivered to Alabama Power’s Joseph M. Farley Nuclear Plant, operated by Southern Nuclear, in the first quarter of 2024 (Westinghouse Electric Company 2024).

Framatome fabricated fuel component via LPBF and successfully introduced them in reactor at Forsmark in Sweden in 2022 (Framatome n.d.). In general, a combination of both techniques could significantly aid the fabrication of reactor specific targeted components and can play a vital role in the large-scale manufacturing of reactor parts.

5.0 Discussion and Conclusions/Recommendations

5.1 LPBF of A709, G91, and G92 Steel Alloys

Main conclusions of LPBF work are:

- Larger scale A709 alloys were successfully printed based on the study from previous year on optimizing the process parameters. The microstructural evolution of the alloy was studied after performing a series of heat treatments. The role of solution annealing the sample led to insights regarding the need for different heat treatments for additively manufactured alloys compared to their wrought counterparts. Precipitation treatment of this alloy, with and without prior solutionizing leads to forming a microstructure which contains different kinds of secondary and tertiary precipitates in the FCC matrix, which significantly enhance the mechanical behavior, as noted in room and elevated temperature tensile testing.
- Similar observations were noted in printing of the ferritic martensitic steels, G91 and G92. A good combination of strength and ductility was obtained in both these alloys, in room temperature tensile testing, by a combination of different heat treatments.
- This exercise proves that the additive manufacturing of the selected Fe-based current reactor materials, either austenitic stainless steel or ferritic/martensitic steels is feasible, and more work needs to be done in order to understand the microstructure evolution during the depositions and also to further optimize the final microstructures.

Future LPBF work recommendations:

- FY25 will focus on further understanding the microstructure evolution and mechanical behavior (room and elevated temperature) of additively manufactured samples compared to the wrought materials. Main focus will be given to alloys A709 and Grade-92.

5.2 LP-DED of A709, G91, and G92 Steel Alloys

Main conclusions of LP-DED work are:

- The parametric study performed as part to the AMMT campaign, identified the processing window for the G91 and G92 steels, and tensile samples were fabricated with the optimized parameters. G91 tensile samples were fabricated using a laser power of 500 W, a scan speed of 600 mm/min, and a hatch spacing of 0.9 mm. G92 tensile samples were fabricated using a laser power of 500 W, a scan speed of 700 mm/min, and a hatch spacing of 0.9 mm.
- A chemical-composition-based ML model is used to predict the tendency of balling defect formation and the porosity in alloys in laser-based AM. The coupled ML and FLOW-3D results have provided insights into the impact of the alloy composition, particularly the carbon content, on the printability of SS316L and SS316H during AM processes.

Future work recommendations:

- The Flow-3D software will be coupled with ML for extensive research on the role of the chemical composition on the printability in the DED process.
- The FY-25 work will focus on DED prints of A709 and G92 for mechanical testing. Further optimization of process parameter will take place based on this FY results. The microstructural and mechanical testing data will be compared with that of LPBF and conventionally fabricated parts.

- For DED A709, solution anneal treatment at a minimum temperature of 1150°C for 10 hours will be implemented followed by air cooling. The precipitation treatment (PT) will be carried out at 775°C for 10 hours in air followed by air cooling (Mahajan et al. 2023). Future study will focus on room-temperature tensile testing for DED fabricated A709 and G92 alloy. In addition, detailed electron microscopy analyses after the heat treatments and tensile testing also fall within the work scope.
- For DED G92, solution anneal treatment at 1080°C will be carried out. G92 is being pursued because of its improved properties compared to G91. Detailed microstructural analysis after heat treatments and mechanical testing will be carried out.

5.3 Comparison between LPBF- and LP-DED-Processed A709, G91, and G92 Steels

It should be noted that the research body is lagging one year behind the LPBF research, as funding and therefore research started only FY24. Therefore, full comparisons of performance could not be completed at this time.

It is also important to understand the role of processing routes on the overall microstructure of the samples printed to assess the final mechanical behavior and subsequently the application to which these parts can be used. As the differences in the overall processes has already been highlighted in the previous sections, this section will focus on the as deposited samples of the three alloys worked on in the current report and following are the main observations:

- A709 Austenitic Stainless Steel: Upon inspection of both DED and LPBF of A709 alloy in its as-deposited condition, it is revealed that they both have single phase FCC crystal structure. The presence of cell boundaries, a typical feature in austenitic stainless steels, is also noted in both the samples. The main differences between the two processes are more observable when looking at the grain sizes based on the EBSD IPF maps. The DED sample has longer/more elongated grains compared to the LPBF processed sample. This could lead to more anisotropy when tested along the build direction as compared to testing across the build direction.
- G91 & G92 Ferritic/Martensitic Steel: In the case of the F/M steels, the difference between the two processes seems to be more pronounced. In the case of the LPBF sample, for the as-deposited conditions, the microstructure seems to show more than a single-phase BCC. Smaller precipitates, most likely theta, along with the presence of martensite like laths are also observed in this sample. These features can be delineated based on the melt pool of the laser. For the DED samples, while the SEM imaging and EBSD IPF maps show what appear to be martensite-like laths, based on the XRD, only BCC phase was noted. It should be mentioned here that, the BCT phase (martensite) has an overlap with the BCC phase, so it possible that we might not be able to see the martensite phase even if its present.

A brief preliminary overview is given on some of the business value consideration that will need to be given for deployment of these AM techniques and decision-making regarding choices of the type of product-AM technique combination. While recognizing that information has been scarce and not been quantified nor validated, it will be challenging to show a promising business value for developers. Adding also that establishing supply chains, and more specifically, understanding the supply chain gaps, detailed evaluation and economic studies would need to be addressed with urgency in the nuclear community by economic and systems specialists.

Finally, it is concluded that all three material types can be to be manufactured using both LPBF and LP-DED processes. While fully recognizing that the process development optimization was conducted within a small parameter window, further improvements for robustness are possible. Different geometries may also necessitate modifications to the parameters and needs to be confirmed for different geometries and size scales. All mechanical properties and their relationship with post heat treatment have not been fully examined. It is recommended that these analyses be completed before making a final decision. It is recommended that future studies focus on A709 and Grade 92 only, to have focus on one austenitic and one ferritic/martensitic material type.

This research work performed at ANL and PNNL is also well published and presented: (1) one invited conference talk, (2) two accepted conference presentations, (3) one peer reviewed paper published in the reputable Materialia, and (4) one paper already submitted and three being drafted.

6.0 Deliverables

Publications:

- Ankit Roy, Andrew Swope, Ram Devanathan, and Isabella J. Van Rooyen. "Chemical composition-based machine learning model to predict defect formation in additive manufacturing." *Materialia* 33 (2024): 102041.
- Journal: Materials Today, On the properties of oxide dispersion strengthened Fe-Cr-Al-0.3Zr-0.3Y_2O_3 fabricated using laser powder bed fusion additive manufacturing, Chinthaka M Silva, Holden Hyer; Tanvi A Ajantiwalay; Shalini Tripathi; Angel Ortiz; Quin R. S. Miller; Nathan Canfield; Subhashish Meher; Sebastien Dryepondt; Isabella J van Rooyen [Submitted]

Future Publications:

- Currently working on submitting the manuscript titled, “Laser Powder Bed Fusion of High Strength Austenitic Alloy, A709” by Mantri et al.
- Currently working on submitting a manuscript titled, “Effect of Solution Annealing on Microstructure Evolution and Mechanical Behavior of Additive Manufactured Austenitic Stainless Steel” by Mantri et al.
- Working title for future publication: “Laser Directed Energy Deposition based Additive Manufacturing of Stainless Steels for Nuclear Applications: Process Development and Characterization Isabella van Rooyen, Subhashish Meher, Asif Mahmud, Peter Renner, John Snitzer, Xiaoyuan Lou

Invited Talk:

- Gave an invited talk at TMS 2023, Orlando, Florida on “Additive Manufacturing of Ferritic/Martensitic Steels for Nuclear Applications” by Mantri et al.

Conference Presentation:

- Ankit Roy, Stephanie Barbara Lawson, Mohan Sai Kiran Kumar Yadav Nartu, Somayeh Pasebani and Isabella J. van Rooyen, Chemical composition-based machine learning model to predict defect formation in additive manufacturing, MS & T 2024, October 7–October 9, 2024, Pittsburgh, PA, USA.
- Subhashish Meher, Asif Mahmud, Peter Renner, German Valenzuela, John Snitzer, Xiaoyuan Lou, Isabella van Rooyen, “Additive Manufacturing and Characterization of A709 Stainless Steels for Nuclear Applications”, TMS 2025, Las Vegas, NV.

Milestone Reports:

- Meher, S., Ankit Roy, Asif Mahmud, Peter A Renner, Chinthaka Silva, Mohan SKKY Nartu, Ariel Rieffer, German A Valenzuela, Isabella J van Rooyen. 2024. Studies on Printability Methodologies and Directed-Energy-Deposition-Fabricated Iron Alloys for Nuclear Applications, PNNL-36408. M3CT-24PN1304051, August 2024
- Mantri, S. A., Xuan Zhang, Wei-Ying Chen. 2024. Laser Powder Bed Fusion of Steels for Nuclear Applications. ANL-AMMT-017, August 2024.

7.0 References

A213/A213M − 19a Standard Specification for Seamless Ferritic and Austenitic Alloy-Steel Boiler, Superheater, and Heat-Exchanger Tubes 1.

Abe, Fujio. 2008. "Precipitate design for creep strengthening of 9% Cr tempered martensitic steel for ultra-supercritical power plants." Science and Technology of Advanced Materials 9. doi: 10.1088/1468-6996/9/1/013002.

Alamos, Fernando J., Jessica Schiltz, Kirsten Kozlovsky, Ross Attardo, Charles Tomonto, Tom Pelletiers, and Steven R. Schmid. 2020. "Effect of powder reuse on mechanical properties of Ti-6Al-4V produced through selective laser melting." International Journal of Refractory Metals and Hard Materials 91. doi: 10.1016/j.ijrmhm.2020.105273.

Alcisto, J., A. Enriquez, H. Garcia, S. Hinkson, T. Steelman, E. Silverman, P. Valdovino, H. Gigerenzer, J. Foyos, J. Ogren, J. Dorey, K. Karg, T. McDonald, and O. S. Es-Said. 2010. "Tensile Properties and Microstructures of Laser-Formed Ti-6Al-4V." Journal of Materials Engineering and Performance 20 (2):203-212. doi: 10.1007/s11665-010-9670-9.

Babuska, Tomas F., Brandon A. Krick, Donald F. Susan, and Andrew B. Kustas. 2021. "Comparison of powder bed fusion and directed energy deposition for tailoring mechanical properties of traditionally brittle alloys." Manufacturing Letters 28:30-34. doi: 10.1016/j.mfglet.2021.02.003.

Baig, Shaharyar, Paul R. Gradl, Shuai Shao, and Nima Shamsaei. 2024. "Temperature dependent tensile behavior of additively manufactured HAYNES® 214: A comparative study between laser powder bed fusion and laser powder directed energy deposition." Journal of Materials Research and Technology 32:1683-1695. doi: 10.1016/j.jmrt.2024.08.031.

Bertoli, S., Umberto, Alexander J. Wolfer, Manyalibo J. Matthews, Jean-Pierre R. Delplanque, and Julie M. Schoenung. 2017a. "On the limitations of Volumetric Energy Density as a design parameter for Selective Laser Melting." Materials & Design 113:331-340. doi: 10.1016/j.matdes.2016.10.037.

Bertoli, S., Umberto, Gabe Guss, Sheldon Wu, Manyalibo J. Matthews, and Julie M. Schoenung. 2017b. "In-situ characterization of laser-powder interaction and cooling rates through high-speed imaging of powder bed fusion additive manufacturing." Materials & Design 135:385-396. doi: 10.1016/j.matdes.2017.09.044.

Betzler, B. R., B. J. Ade, A. J. Wysocki, P. C. Chesser, and K. A. Terrani. 2020. "Transformational Challenge Reactor Agile Design Enabled by Additive Manufacturing." 2020 ANS Winter Meeting and Nuclear Technology Expo.

Busachi, Alessandro, John Erkoyuncu, Paul Colegrove, Filomeno Martina, Chris Watts, and Richard Drake. 2017. "A review of Additive Manufacturing technology and Cost Estimation techniques for the defence sector." CIRP Journal of Manufacturing Science and Technology 19:117-128. doi: 10.1016/j.cirpj.2017.07.001.

Chen, Z. Wei, P. Wei, S. Chen, B. Lu, J. Du, J. Li, S. Zhang, Experimental Research on Selective Laser Melting AlSi10Mg Alloys: Process, Densification and Performance, Journal of Materials Engineering and Performance 26(12) (2017) 5897-5905.

Chowdhury, Sohini, N. Yadaiah, Chander Prakash, Seeram Ramakrishna, Saurav Dixit, Lovi Raj Gupta, and Dharam Buddhi. 2022. "Laser powder bed fusion: a state-of-the-art review of the technology, materials, properties & defects, and numerical modelling." Journal of Materials Research and Technology 20:2109-2172. doi: 10.1016/j.jmrt.2022.07.121.

Dawes, Jason, Robert Bowerman, and Ross Trepleton. 2015. "Introduction to the Additive Manufacturing Powder Metallurgy Supply Chain." Johnson Matthey Technology Review 59 (3):243-256. doi: 10.1595/205651315x688686.

DebRoy, T., H. L. Wei, J. S. Zuback, T. Mukherjee, J. W. Elmer, J. O. Milewski, A. M. Beese, A. Wilson-Heid, A. De, and W. Zhang. 2018. "Additive manufacturing of metallic components – Process, structure and properties." Progress in Materials Science 92:112-224. doi: 10.1016/j.pmatsci.2017.10.001.

Delacroix, Timothée, Fernando Lomello, Frédéric Schuster, Hicham Maskrot, and Jean-Paul Garandet. 2022. "Influence of powder recycling on 316L stainless steel feedstocks and printed parts in laser powder bed fusion." Additive Manufacturing 50. doi: 10.1016/j.addma.2021.102553.

Dicknes, P., and N. Hopkinson. 2003. "Analysis of rapid manufacturing—using layer manufacturing processes for production." Proceedings of the Institution of Mechanical Engineers, Part C: Journal of Mechanical Engineering Science.

Ding, Rengen, Jin Yan, Hangyue Li, Suyang Yu, Afsaneh Rabiei, and Paul Bowen. 2019. "Microstructural evolution of Alloy 709 during aging." Materials Characterization 154:400-423. doi: 10.1016/j.matchar.2019.06.018.

Eftink, Benjamin P., Daniel A. Vega, Osman El Atwani, David J. Sprouster, Yung Suk J. Yoo, Todd E. Steckley, Eda Aydogan, Carl M. Cady, Mohamad Al-Sheikhly, Thomas J. Lienert, and Stuart A. Maloy. 2021. "Tensile properties and microstructure of additively manufactured Grade 91 steel for nuclear applications." Journal of Nuclear Materials 544. doi: 10.1016/j.jnucmat.2020.152723.

El-Atwani, O., B. P. Eftink, C. M. Cady, D. R. Coughlin, M. M. Schneider, and S. A. Maloy. 2021. "Enhanced mechanical properties of additive manufactured Grade 91 steel." Scripta Materialia 199. doi: 10.1016/j.scriptamat.2021.113888.

Fan, Jinming, Yueyue Zhu, Weiyi Wang, Ke Chen, Andrew Godfrey, Tianbo Yu, and Xiaoxu Huang. 2024. "Recovery of dislocation cell structures in 316L stainless steel manufactured by selective laser melting." Journal of Materials Research and Technology 30:9472-9480. doi: 10.1016/j.jmrt.2024.05.269.

Framatome. n.d. "Framatome accelerates the industrial implementation of Advanced Additive Manufacturing." accessed September 19.2024 https://www.framatome.com/en/expertise/advanced-additive-manufacturing/.

Ghods, S., R. Schur, E. Schultz, R. Pahuja, A. Montelione, C. Wisdom, D. Arola, and M. Ramulu. 2021. "Powder reuse and its contribution to porosity in additive manufacturing of Ti6Al4V." Materialia 15. doi: 10.1016/j.mtla.2020.100992.

Gisario, Annamaria, Michele Kazarian, Filomeno Martina, and Mehrshad Mehrpouya. 2019. "Metal additive manufacturing in the commercial aviation industry: A review." Journal of Manufacturing Systems 53:124-149. doi: 10.1016/j.jmsy.2019.08.005.

Gnaase, Stefan, Dennis Niggemeyer, Dennis Lehnert, Christian Bödger, and Thomas Tröster. 2023. "Comparative Study of the Influence of Heat Treatment and Additive Manufacturing Process (LMD & L-PBF) on the Mechanical Properties of Specimens Manufactured from 1.2709." Crystals 13 (2). doi: 10.3390/cryst13020157.

Gradl, Paul, Darren C. Tinker, Alison Park, Omar R. Mireles, Marissa Garcia, Ryan Wilkerson, and Christopher McKinney. 2022. "Robust Metal Additive Manufacturing Process Selection and Development for Aerospace Components." Journal of Materials Engineering and Performance 31 (8):6013-6044. doi: 10.1007/s11665-022-06850-0.

Gräning, T. and N. Sridharan (2022). "Benchmarking a 9Cr-2WVTa Reduced Activation Ferritic Martensitic Steel Fabricated via Additive Manufacturing." Metals 12(2): 342.

Green, T. M. Kelsy, Niyanth Sridharan, Xiang Chen, and Kevin G. Field. 2022. "Effect of N2- and CO2-containing shielding gases on composition modification and carbonitride precipitation in wire arc additive manufactured grade 91 steel." Additive Manufacturing 56. doi: 10.1016/j.addma.2022.102854.

Haley, James, Kevin Faraone, Brian Gibson, Joseph Simpson, and Ryan Dehoff. 2021. Review of Advanced Manufacturing Techniques and Qualification for Light -Water Reators: Laser-Directed Energy Deposition Additive Manufacturing OAK RIDGE NATIONAL LABORATORY

Hartmann, T. and Ram Devanathan. 2021. Materials Scorecards, Phase 1 (Advanced Materials and Manufacturing Technology). Pacific Northwest National Laboratory.

Hartmann, Thomas, Stuart Maloy, and Mageshwari Komarasamy. 2022. Material Scorecards, Phase 2 Pacific Northwest National Laboratory.

Hasegawa, Y. 2014. "Grade 92 creep-strength-enhanced ferritic steel." In Coal Power Plant Materials and Life Assessment, 52-86.

Hatakeyama, Tomotaka, Kota Sawada, Masaru Suzuki, and Makoto Watanabe. 2023. "Microstructure development of modified 9Cr-1Mo steel during laser powder bed fusion and heat treatment." Additive Manufacturing 61. doi: 10.1016/j.addma.2022.103350.

Herzog, Dirk, Vanessa Seyda, Eric Wycisk, and Claus Emmelmann. 2016. "Additive manufacturing of metals." Acta Materialia 117:371-392. doi: 10.1016/j.actamat.2016.07.019.

King, W. E., A. T. Anderson, R. M. Ferencz, N. E. Hodge, C. Kamath, S. A. Khairallah, and A. M. Rubenchik. 2015. "Laser powder bed fusion additive manufacturing of metals; physics, computational, and materials challenges." Applied Physics Reviews 2 (4). doi: 10.1063/1.4937809.

Klueh, R. L., and A. T. Nelson. 2007. "Ferritic/martensitic steels for next-generation reactors." Journal of Nuclear Materials 371 (1-3):37-52. doi: 10.1016/j.jnucmat.2007.05.005.

Lewandowski, John J., and Mohsen Seifi. 2016. "Metal Additive Manufacturing: A Review of Mechanical Properties." Annual Review of Materials Research 46 (1):151-186. doi: 10.1146/annurev-matsci-070115-032024.

Li, Kun, Michael A. Klecka, Shuying Chen, and Wei Xiong. 2021. "Wire-arc additive manufacturing and post-heat treatment optimization on microstructure and mechanical properties of Grade 91 steel." *Additive Manufacturing* 37. doi: 10.1016/j.addma.2020.101734.

Li, M., D. Andersson, R. Dehoff, A. Jokisaari, I. van Rooyen, Dirk Cairns-Gallimore. 2023. "DOE-NE Advanced Materials and Manufacturing Technologies AMMT) Program Overview."

Lienert, T. J. and S. A. Maloy (2017). Laser Additive Manufacturing of F/M Steels for Radiation Tolerant Nuclear Components. United States: Medium: ED; Size: 19 p.

Lohse, C., Abdalla Abou-Jaoude, William D. Jenson, Ian Prado. April 2023. Advanced Reactor Supply Chain Assessment, GAIN Report. In NL/RPT-23-70928: Idaho National Labaratory.

Mahajan, H. P., Y. Wang, Z. Feng, X. Zhang and T.-L. Sham (2023). A summary of the mechanical properties data developed in FY 2023 by ANL, INL and ORNL to support the data package development for the A709 Code Case. United States: Medium: ED.

Mantri,S.A., X. Zhang. 2023. Evaluation of LPBF Steels for Nuclear Applications. Argonne National Laboratory.

Mantri, S. A., X. Zhang, Wei-Ying Chen W-Y., 2024. Laser Powder Bed Fusion of Steels for Nuclear Applications. ANL-AMMT-017, August 2024.

Meher, S., Chinthaka Silva, Mohan Sai Kiran Kumar Yadav Nartu, Ankit Roy, William Frazier, Mageswari Komarasamy, Tanvi Ajantiwalay, Shalini Tripathi, Jonathan Wierschke, Nathan Canfield, Isabella van Rooyen. 2023. Evaluation of Printability Methodologies and Feasibility to Down-Select LBPF Steel and Other Materials for Nuclear Applications. PNNL-34601. July 2023, Pacific Northwest National Laboratory.

Meher, S., Ankit Roy, Asif Mahmud, Peter A Renner, Mohan Sai Kiran Kumar Yadav Nartu, Chinthaka Silva, Ariel Rieffer, German A Valenzuela, Isabella J van Rooyen. 2024. Studies on Printability Methodologies and Directed-Energy-Deposition-Fabricated Iron Alloys for Nuclear Applications. PNNL-36408. M3CT-24PN1304051, August 2024Pacific Northwest National Laboratory.

Moghimian, Pouya, Thomas Poirié, Mahdi Habibnejad-Korayem, Javier Arreguin Zavala, Jens Kroeger, Frédéric Marion, and Frédéric Larouche. 2021. "Metal powders in additive manufacturing: A review on reusability and recyclability of common titanium, nickel and aluminum alloys." Additive Manufacturing 43. doi: 10.1016/j.addma.2021.102017.

Nag, Soumya, Mithulan Paramanathan, Fred List, Thomas Feldhausen, Andrzej Nycz, Bill Carter, Dennis Brown, Lauren Heinrich, Kenton Blane Fillingim, Luke Meyer, Brian Jordan, Jason Mayeur, Peeyush Nandwana, Yousub Lee, James Haley, and Vincent Paqui. 2023. In Situ Monitoring Assisted LargeScale Additive Manufacturing of MildSteel and 316 Alloys for Nuclear Applications. OAK RIDGE NATIONAL LABORATORY.

Natesan, K., and T.-L. Sham. 2017. "Code Qualification Plan for an Advanced Austenitic Stainless Steel, Alloy 709, for Sodium Fast Reactor Structural Applications." IAEA-CN245-074.

Niaki, M. K., F. Nonino, G. Palombi, and S. A. Torabi. 2019. "Economic sustainability of additive manufacturing Contextual factors driving its performance in rapid prototyping." Journal of Manufacturing Technology Management 30 (2):353-365. doi: 10.1108/Jmtm-05-2018-0131.

Robin, I. K., D. J. Sprouster, N. Sridharan, L. L. Snead, and S. J. Zinkle. 2024. "Synchrotron based investigation of anisotropy and microstructure of wire arc additive manufactured Grade 91 steel." Journal of Materials Research and Technology-Jmr&T 29:5010-5021. doi: 10.1016/j.jmrt.2024.02.230.

Roy, A., A. Swope, R. Devanathan, I.J. Van Rooyen. 2024. Chemical composition based machine learning model to predict defect formation in additive manufacturing, Materialia (2024) 102041.

Rupp, R., Yanli Wang, Xuan Zhang, Ting-Leung Sham. 2021. Integrated FY-2021 Elevated Temperature Mechanical-Testing Results for Alloy 709 Code Case. Idaho National Laboratory.

Sames, W. J., F. A. List, S. Pannala, R. R. Dehoff, and S. S. Babu. 2016. "The metallurgy and processing science of metal additive manufacturing." International Materials Reviews 61 (5):315-360. doi: 10.1080/09506608.2015.1116649.

Samuha, S., J. Bickel, T. Mukherjee, T. DebRoy, T. J. Lienert, S. A. Maloy, C. R. Lear, and P. Hosemann. 2023. "Mechanical performance and microstructure of the grade 91 stainless steel produced via Directed Energy deposition laser technique." Materials & Design 227. doi: 10.1016/j.matdes.2023.111804.

Santecchia, Eleonora, Stefano Spigarelli, and Marcello Cabibbo. 2020. "Material Reuse in Laser Powder Bed Fusion: Side Effects of the Laser—Metal Powder Interaction." Metals 10 (3). doi: 10.3390/met10030341.

Selcuk, C. 2011. "Laser metal deposition for powder metallurgy parts." Powder Metallurgy 54 (2):94-99. doi: 10.1179/174329011x12977874589924.

Sham, T., Yanli Wang, Ryann Bass, Xuan Zhang. 2022. A709 Qualification Plan Update and Mechanical Properties Data Assessment.

Shamsaei, Nima, Aref Yadollahi, Linkan Bian, and Scott M. Thompson. 2015. "An overview of Direct Laser Deposition for additive manufacturing; Part II: Mechanical behavior, process parameter optimization and control." Additive Manufacturing 8:12-35. doi: 10.1016/j.addma.2015.07.002.

Shingledecker, J., D. Gandy, and M. Albert. June 2022. Supply Chain Challenges and Opportunities for Structural Components in Advanced Energy Systems: EPRI Workshop Summary. EPRI.

Song, Xu, Stefanie Feih, Wei Zhai, Chen-Nan Sun, Feng Li, Raj Maiti, Jun Wei, Yangzhan Yang, Victor Oancea, Leon Romano Brandt, and Alexander M. Korsunsky. 2020. "Advances in additive manufacturing process simulation: Residual stresses and distortion predictions in complex metallic components." Materials & Design 193. doi: 10.1016/j.matdes.2020.108779.

Sourmail, T. 2005. "Near equiatomic FeCo alloys: Constitution, mechanical and magnetic properties." Progress in Materials Science 50 (7):816-880. doi: 10.1016/j.pmatsci.2005.04.001.

Sourmail, T., and H. K. D. H. Bhadeshia. 2005. "Microstructural evolution in two variants of NF709 at 1023 and 1073 K." Metallurgical and Materials Transactions A 36 (1):23-34. doi: 10.1007/s11661-005-0135-y.

Tan, L, M.A. Sokolov, T.-L. Sham. June 2017. "Creep Resistance and Fracture Toughness of Recently-Developed Optimized Grade 92 and Its Weldments for Advanced Fast Reactors." International Conference on Fast Reactors and Related Fuel Cycles: Next Generation Nuclear Systems for Sustainable Development (FR17), Yekaterinburg, Russia.

Tan, L. 2018. Assessment of the Propensity of Low Creep Ductility for Optimized Grade 92 Steel. OAK RIDGE NATIONAL LABORATORY.

Tan, L., Xiang Chen. 2021. LONG-TERM THERMAL AGING EFFECT EVALUATION FOR GRADE 92 AND 316L AT THE LWR RELEVANT TEMPERATURE. OAK RIDGE NATIONAL LABORATORY.

Tan, Lizhen, Weicheng Zhong, Ying Yang, Kevin G. Field, Niyanth Sridharan, and Andrew T. Nelson. 2022. "Creep behavior of an additively manufactured 9Cr steel in the as-built condition." Journal of Nuclear Materials 570. doi: 10.1016/j.jnucmat.2022.153943.

Tavcar, Joze, and Axel Nordin. 2021. "Multi-Criteria Assessment and Process Selection Model for Additive Manufacturing in the Conceptual Phase of Design." Proceedings of the Design Society.

Thomas, D. 2016. "Costs, Benefits, and Adoption of Additive Manufacturing: A Supply Chain Perspective." Int J Adv Manuf Technol 85 (5-8):1857-1876. doi: 10.1007/s00170-015-7973-6.

Thomas, Douglas S., and Stanley W. Gilbert. 2014. Costs and Cost Effectiveness of Additive Manufacturing.

Thompson, Scott M., Linkan Bian, Nima Shamsaei, and Aref Yadollahi. 2015. "An overview of Direct Laser Deposition for additive manufacturing; Part I: Transport phenomena, modeling and diagnostics." Additive Manufacturing 8:36-62. doi: 10.1016/j.addma.2015.07.001.

Van Rooyen, I. J., 2024a. Development of Advanced Manufactured Alloys for Nuclear Structural Materials AMMT Industry Workshop, Collaborative Computing Center, Idaho National Laboratory, Idaho Falls, July 10-11, 2024

Van Rooyen, I. J., 2024b. “GIF AMME Working Group”, IAEA Technical Meeting on the Deployment of Advanced Manufacturing Solutions for the Nuclear Power Industry, 19-22 August 2024

Warner, James H., Simon P. Ringer, and Gwénaëlle Proust. 2024. "Strategies for metallic powder reuse in powder bed fusion: A review." Journal of Manufacturing Processes 110:263-290. doi: 10.1016/j.jmapro.2023.12.066.

Wang, Y., Wei Zhang, Yanli Wang, Zhili Feng. 2024. "MICROSTRUCTURE AND CREEP PERFORMANCE OF WIRE ARC ADDITIVE MANUFACTURED GRADE 91 STEEL." 2024 ASME Pressure Vessels and Piping Conference, Bellevue, Washington, USA.

Westinghouse Electric Company. 2024. Westinghouse's Additive Manufacturing Innovation Improves Safety and Efficiency in Operating Nuclear Reactors.

Whitt, A., R. Seede, J. Ye, M. Elverud, M. Vaughan, A. Elwany, R. Arroyave and I. Karaman (2023). "A process optimization framework for laser direct energy deposition: Densification, microstructure, and mechanical properties of an Fe Cr alloy." Journal of Manufacturing Processes 85: Medium: X; Size: p. 434-449.

Zach, M., Dane Brashear, Jonah Duran, Łukasz Żrodowski, Bartosz Kalicki, Tomasz Choma, Marcin, and and Steven Adler Sołowiow. 2023. "Spherical powders: Control over the size and morphology of powders for additive manufacturing and enriched stable isotope nuclear targets." EPJ Web of Conferences.

Zhong, Weicheng, Niyanth Sridharan, Dieter Isheim, Kevin G. Field, Ying Yang, Kurt Terrani, and Lizhen Tan. 2021. "Microstructures and mechanical properties of a modified 9Cr ferritic-martensitic steel in the as-built condition after additive manufacturing." Journal of Nuclear Materials 545. doi: 10.1016/j.jnucmat.2020.152742.

Pacific Northwest National Laboratory

902 Battelle Boulevard
P.O. Box 999
Richland, WA 99354

1-888-375-PNNL (7665)

www.pnnl.gov